Supplemental Information for "On predictability of slip, rupture geometry, and rupture speed of the M_w7.8 2025 Mandalay (Myanmar) Earthquake"

Thomas Ulrich[1†], Xiaoyu Zou[2†], Mathilde Marchandon[1], Nico Schliwa[1], Fengzhou Tan[2], Alice-Agnes Gabriel[1,2*], Wenyuan Fan[2], Peter Shearer[2], Myo Thant[3], Tha Zin Htet Tin[4], Eric O. Lindsey[5], Yuri Fialko[2]

[1*]Department of Earth and Environmental Sciences, Ludwig-Maximilians-Universität München, Munich, 80539, Germany.
[2]Institute of Geophysics and Planetary Physics, Scripps Institution of Oceanography, University of California San Diego, La Jolla, 92093, CA, USA.
[3]Myanmar Institute of Earth and Planetary Sciences, Yangon, Myanmar.
[4]Department of Geology, University of Yangon, Yangon, Myanmar.
[5]Department of Earth and Planetary Sciences, University of New Mexico, Albuquerque, 87131, NM, USA.

*Corresponding author(s). E-mail(s): algabriel@ucsd.edu;
Contributing authors: thomas.ulrich@lmu.de; x3zou@ucsd.edu; mathilde.marchandon@lmu.de; nico.schliwa@lmu.de; f4tan@ucsd.edu; wenyuanfan@ucsd.edu; pshearer@ucsd.edu; myothant05@gmail.com; thazinhtettin@gmail.com; eol@unm.edu; yfialko@ucsd.edu;
[†]These authors contributed equally to this work.

Contents of this file

Text S1. Space Geodetic Data Processing

We use Synthetic Aperture Radar (SAR) data acquired by Sentinel-1A satellite in TOPS mode (ascending tracks 70 and 143; descending tracks 33 and 106) and ALOS-2 satellite in ScanSAR mode (ascending track 152; descending tracks 41 and 42). The respective acquisition dates are listed in Table S1. All data are processed using GMTSAR[1] and the Shuttle Radar Topography Mission (SRTM) digital elevation model with 30 m postings[2]. For the Sentinel-1A data, we estimate azimuth offsets using pixel-tracking. We cross-correlate the Single Look Complex (SLC) images with a sampling interval of 8 pixels in azimuth and range. To improve the signal to noise ratio, we only select pixels for which the calculated azimuth offset is less than 10 meters. We then use the fault trace projected in the radar (range-Doppler) coordinates to split the scene into two parts. For each part, we fit a low-order 2-D spline to a scattered set of pixels using a surface modeling tool *gridfit*[3]. We then remove pixels with offsets that deviate more than 2 m from the best-fit spline. The remaining set of pixels is filtered using a Gaussian filter with wavelength of 0.5 km. The two parts of the image are recombined and projected from radar to geographic coordinates. Separate processing of the 2 parts is meant to avoid filtering of averaging of discontinuous data along the fault trace. The resulting offsets are shown in Fig. S2. We do not use interferometric phase from Sentinel-1A measurements because it is highly decorrelated, especially in the near field (5-10 km) of the earthquake rupture.

For the ALOS-2 data, we process 3 ScanSAR frames from each track spanning the earthquake rupture. Each frame consists of 5 sub-swathes that are co-registered, filtered, and merged into a full frame. The merged frames are unwrapped using the branch-cut algorithm[4]. This allows to confidently unwrap the radar phase in frames that cover the rupture tips. For the central frames that are completely crossed by the $\sim$500 km long earthquake rupture, we use data from the overlap areas between the adjacent frames to solve for the 2π ambiguity, and manually bridge the phase across the fault trace. Finally, we merge the 3 frames by minimizing phase difference in the overlap areas. Fig. S3a shows an example of interferometric phase from 3 merged frames from the descending track 41. The phase data are dominated by a long-wavelength ramp, most likely due to ionospheric variability. Noting that coseismic displacements are expected to vanish at distances of the order of 50-100 km away from the fault trace, we take advantage of the wide-swath capability of ALOS-2 to remove the long-wavelength contribution due to ionosphere. We resample the merged unwrapped interferogram to grid spacing of 1 km, mask out data within $\sim$100 km from the fault trace, and fit a tension spline to the remaining set of pixels. The best-fit spline surface is then upsampled and subtracted from the original data at full resolution. Fig. S3b shows the interferometric phase upon the respective correction. The coseismic signal is clearly visible, along with some fringes that likely represent uncorrected tropospheric and ionospheric artifacts. The phase remains coherent all the way to the rupture trace, due to a larger wavelength of the ALOS-2 radar (0.23 m, compared to 0.06 m for Sentinel-1A satellite). Line of sight (LOS) displacements obtained from the merged, unwrapped, and de-trended ALOS-2 interferograms are shown in Fig. S4 While the predominantly strike-slip sense of motion on a North-South trending earthquake rupture implies that only a small fraction of strike-slip motion can be observed along the satellite LOS, interferometric data nevertheless represent a valuable constraint because they have a high sensitivity to the dip-slip component, and therefore reduce possible trade-offs between the strike- and dip-slip. Also, because of the large magnitude of strike-slip, a LOS projection as small as several percents still has a signal to noise ratio that is larger than that in pixel offsets (Figs. S2, S4).

The azimuth offset and LOS displacement data (Figs. S2, S4) are sub-sampled using a quad-tree algorithm[5–7] to reduce the computational cost and achieve a better model resolution. The unit-look vectors are computed by averaging the original values in the same groups of pixels as used for sub-sampling the phase and pixel offset data.

In addition to the LOS and azimuth displacements derived from the SAR images, we also measure the horizontal surface displacement field of the Mandalay earthquake by cross-correlating optical images collected by Sentinel-2 satellite. The Sentinel-2 images have a pixel size of about 10 m. Twelve pairs of pre-earthquake (2025/03/25-27) and post-earthquake (2025/03/30 and 2025/04/01) images are needed to cover the 500 km long rupture area (Table S1). As the Sentinel-2 images are provided already orthorectified, no geometrical correction is applied prior the correlation. We use the phase correlator of the software package COSI-Corr[8–10] with a multiscale sliding correlation window of 128 to 64 pixels and a measurement step of 6 pixels. We discard from the resulting 60 m East-West (EW) and North-South (NS) displacement fields any data point having a signal-to-noise ratio lower than 0.95 and a displacement amplitude higher than 10 m. Finally, we smooth the EW and NS displacement fields using a median filter with a 5x5 pixels window.

Text S2. Measurement of Surface Fault Offsets

Fault-parallel offsets are obtained from the Sentinel-2 horizontal displacement field using a series of uniformly distributed, fault-perpendicular stacked profiles. Each profile spans 70 km long and is laterally averaged over a width of 2 km to enhance the signal-to-noise ratio. Displacement offsets are measured by performing linear regression fits to the displacement data on either side of the fault trace and computing the offset as the difference between the extrapolated values of the regressions at the fault. Associated uncertainties are estimated by calculating the root mean square (RMS) of the 1-sigma standard deviations of the regression fits on both sides of the fault. In total, we measured 258 profiles. Fault zone width is also quantified by measuring the distance between the inflection points in the displacement profile on either side of the fault.

Text S3. Retrieval of 3 Orthogonal Components of Surface Displacements from SAR Data

The azimuth offsets and LOS displacements from 7 different satellite tracks (Figs. S2, S4) are used to retrieve the three orthogonal components of the coseismic displacement field[11;12]. The respective geocoded data sets are first resampled onto a common grid. To reduce speckle, the azimuth offsets are filtered using a 1 km Gaussian filter. For each pixel of a common grid we form a system of linear equations by adding the respective unit look vectors as rows to the design matrix and the observed quantity to the data vector. The resulting system is solved using least squares for the three orthogonal components of the displacement vector if the following two conditions are met: (i) more than two observations from different data sets are available for a given pixel and (ii) a condition number of the design matrix is less than some threshold (100 in our calculations). The first condition ensures that the system is not under-determined; the second condition ensures that there is sufficient diversity in the look angles (that is, the solution is not highly unstable with respect to the data errors). The resulting horizontal component of the displacement field is shown in Fig. 1b in the main text.

Text S4. A 1-D model of S-wave Velocity and Shear Modulus for the Sagaing Fault

We construct a depth-dependent S-wave velocity model using depth-averaged, binned shear wave velocity data from stations within approximately 50 km of the Sagaing Fault[13]. The bin boundaries are determined by identifying depths where the cumulative absolute change in velocity exhibits local maxima. The shear modulus corresponding to each depth layer (bin) is calculated based on the empirical relationship between seismic wave velocity and density[14]. The resulting 1-D S-wave velocity and shear modulus distributions as a function of depth are shown in Fig. S5.

Text S5. Estimation of Subsurface Fault Geometry from Geodetic Data

To constrain the three-dimensional geometry of the Sagaing Fault, we first digitize the surface trace of the 2025 earthquake rupture using azimuth offsets derived from Sentinel-1 data, and the NS component of horizontal displacements derived from Sentinel-2 data. We then partition the rupture trace into seven linear segments (Fig S6a). Except for the relatively short segment 1 which represents a small kink near the northern end of the earthquake rupture, the rest of the segments (segments 2–7) are nearly equal in length, about 80 km each. Segments 2–7 are modeled as planar faults sub-divided into rectangular dislocations. For every segment, we extract 60 km wide swathes of data centered on, and perpendicular to the segment, and invert them for the best-fit slip distribution using SlipSolve algorithm [15]. The algorithm calculates Green's functions assuming a layered elastic half-space [16], using a 1-D rigidity model shown in Fig. S5b. For each segment, we perform several inversions for different assumed dip angles. Resulting data misfits are shown in Fig. S6. Dip angles that yield a minimum misfit value are taken to be representative of the respective segments. We do not perform a separate grid search for segment 1, as it is too short for a 2-D approximation. Instead, we constrain the dip of segment 1 to be equal to that of segment 2. We then project each planar sub-fault using its inferred dip angle to a depth of 25 km. Finally, we fit a smooth continuous 3-D surface to a set of points spanning the fault trace and (on average) the individual sub-faults 1-7 [17]. The resulting surface has a helical geometry with a dip angle varying smoothly along strike, as illustrated in Fig. 2a in the main text.

Text S6. Inversion of Geodetic Data for Static Slip Model

Inversions of coseismic displacements for the subsurface slip distribution typically approximate faults as a superposition of dislocations [5;6;18]. The most popular choice is a rectangular dislocation in a homogeneous [19] or layered [16] elastic half-space. Triangular Dislocation Elements (TDE) are generally better suited for approximating complex non-planar surfaces [17;20;21]. However, finite dislocations give rise to an unphysical piece-wise constant ("staircase") approximation of coseismic slip. Here, we use a novel method for inverting surface displacements using piece-wise linear triangular boundary elements in a layered elastic half-space that ensures a continuous slip distribution. As a first step, we tessellate the 3-D curved fault surface (Fig. 2a) to produce a "watertight" mesh of triangular elements. The element size gradually increases from $\sim$1 km at the Earth's surface to $\sim$5 km at the bottom of the fault model (20-25 km), to keep the model resolution matrix close to diagonal [22]. Each triangular element is given by a superposition of equally spaced point sources [17]. The Green's functions for point sources are computed assuming a 1-D rigidity structure shown in Fig. S5b, except for elements at the free surface, for which we use regular TDEs [21] to avoid singularities in the near field of the fault trace. We then calculate Green's functions for the vertices of the triangular elements, imposing a slip of unity at the given vertex, and a linear decrease of slip to zero to the other vertices of all adjacent triangular elements. This is similar to a treatment of triangular elements with linear basis functions in the Finite Element Method [23]. Finally, we solve for slip u at the nodes (vertices of interconnected triangular elements) of the mesh by forming a linear system of equations $Gu = d$, where G is the Green's function matrix, and d is the data vector consisting of sub-sampled Sentinel-1 azimuth offsets and ALOS-2 LOS displacements. Vector u consists of strike-slip and dip-slip components for each node. The matrix G accounts for the projection of the 3-component surface displacement field onto the respective lines of sight or flight directions. We seek the slip distribution u that minimizes a functional

$$F(u, \lambda) = ||Gu - d||_2 + \lambda||\nabla^2 u||_2, \quad (1)$$

where $||.||_2$ is the Euclidean (L_2) norm, ∇^2 is the Laplacian operator that penalizes curvature in the slip distribution and serves as a regularization operator to avoid ill-posedness [24], and λ is the smoothness parameter. The latter is chosen to optimize the trade-off between the model smoothness and fit to the data (Fig. S7). We implement a discrete Laplacian operator on a triangular mesh using an edge-level hybrid scheme: for triangular elements having acute angles, we use a cotangent formula, and mean-value weights otherwise[25]. Assume two nodes i and j share the same edge, ij (Fig. S8); $\theta_{ikj}, \theta_{ilj}$ are the vertex angles opposite to the edge ij; k and l are the vertices of triangles at $\theta_{ikj}, \theta_{ilj}$, and $\mathbf{p}_i, \mathbf{p}_j$ are the 3-D position vectors of nodes i and j,

$$w_{ij} = \begin{cases} \frac{1}{2}\left(\cot\theta_{ikj} + \cot\theta_{ilj}\right), & \text{if } \theta_{ikj}, \theta_{ilj} \in (0, \frac{\pi}{2}) \text{ (both acute)}, \\ \dfrac{\tan(\theta_{kij}/2) + \tan(\theta_{lij}/2) + \tan(\theta_{kji}/2) + \tan(\theta_{lji}/2)}{\|\mathbf{p}_i - \mathbf{p}_j\|}, & \text{otherwise}, \end{cases} \tag{2}$$

where θ_{kij} is an angle between triangle sides ki and ij. The discrete Laplacian operator at a node i is given by[25]

$$\nabla^2 u_i = \frac{1}{S_i}\sum_{j=1}^{N} w_{ij}(u_j - u_i), \tag{3}$$

where S_i is the mixed-Voronoi area[26;27] for node i to provide relative scaling across variable triangle sizes (Fig S8), and N is the total number of nodes immediately adjacent to node i. For each triangle T (vertices i, j and k, with coordinate vectors $\mathbf{p}_i$, $\mathbf{p}_j$ and $\mathbf{p}_k$, and area A_T) that forms the cell area surrounding node i, the area of the respective Voronoi cell is calculated as

$$S_i^{(T)} = \begin{cases} \dfrac{1}{8}\left(\cot\theta_{ijk}\,\|\mathbf{p}_i - \mathbf{p}_k\|^2 + \cot\theta_{ikj}\,\|\mathbf{p}_i - \mathbf{p}_j\|^2\right), & \text{if } T \text{ is non-obtuse}, \\ \dfrac{1}{2}A_T, & \text{if } \theta_{kij} > \frac{\pi}{2} \ \text{ (obtuse at } i), \\ \dfrac{1}{4}A_T, & \text{if } T \text{ is obtuse at } j \text{ or } k. \end{cases} \tag{4}$$

S_i is a union of all Voronoi cells $S_i^{(T)}$ around the node i (Fig. S8).

The design matrix of an inverse problem consists of G and a symmetric, sparse regularization matrix that independently constrains strike- and dip-slip components of u. TDEs at the top of the slip model are constrained to have the same slip as the top nodes of the linear triangular elements immediately below. In addition, we impose "soft" zero-slip conditions at the lateral and bottom boundaries of the mesh[28]. The inversions are performed using SlipSolve package[15]. The best-fit slip model of the 2025 Mandalay earthquake is shown in Fig. S9.

The uncertainties are estimated using a bootstrap method. We perform several inversions using the same parameters, but excluding one of the datasets. Azimuth offsets from Sentinel-1A track D106 are kept in all runs, since this track is well centered on the earthquake rupture. At each node, we take the difference between the maximum and minimum slip values in all of the inversions as uncertainty in the respective component of slip (Fig. S10).

To validate the resolving power of our inverse models, we execute a set of inversions using synthetic data. Using the same fault geometry and the same mesh, we replace each triangular element with analytic TDEs[21]. We then apply a slip distribution that tapers elliptically from the maximum slip of 5 m in the middle of the fault trace to zero at the depth of 17 km, and toward the side ("North" and "South") edges of the mesh. The dip-slip component is zero. We compute surface displacements and project them onto the lines of sight and flight directions corresponding to the Sentinel-1A and ALOS-2 datasets (Figs. S11–S17). To simulate realistic noise, we use residuals (Figs. S11c–S17c) in which we mask out pixels within 3 km from the fault trace and replace them with residuals from the far-field ($>$ 20 km from the fault trace). The respective noise is added to synthetic data, which are then sub-sampled and inverted for the best-fit slip distribution using the same procedure as described above, except the Green's functions are calculated for a homogeneous elastic half-space. The recovered slip distribution closely reproduces the input model in the top 15 km (Fig. S18). Below 15 km, the inverse model somewhat over-predicts the synthetic model due to loss of model resolution.

Text S7. Dynamic rupture modeling approach, fault friction and initial shear stresses

To generate ensembles of 3D dynamic rupture simulations[29], we use the open-source software SeisSol[30]. SeisSol solves the coupled problem of spontaneous dynamic rupture and seismic wave propagation with high-order accuracy in space and time[31]. It implements the Arbitrary high-order accurate DERivative Discontinuous Galerkin method (ADER-DG[32]) and incorporates end-to-end optimization for modern high-performance computing architectures[33–37]. SeisSol has been extensively verified through a broad suite of community benchmark problems designed by the SCEC/USGS Dynamic Rupture Code Verification project[38–40].

We adopt a linear slip-weakening friction law[41;42]. The dynamic friction coefficient is assumed constant at $\mu_\mathrm{d} = 0.15$. The critical slip weakening distance d_c and static friction coefficient μ_s vary across the fault (Fig. S24b, Table S2).

We constrain the geometry and initial shear stresses of all 3D dynamic rupture models using the fault geometry and slip distribution from the geodetic slip model. Kinematic (time-dependent) finite fault models have been previously employed to determine initial parameters for dynamic rupture simulations[43–48]. We use a pseudo-static simulation, hereafter referred to as 'dynamic relaxation simulation' using the same computational mesh and the same fault geometry as the subsequent dynamic rupture simulations[49;50]. We impose the time-independent geodetic slip distribution across the entire fault using a 3 s rise-time Gaussian slip-rate function, applied through an internal boundary condition to determine the corresponding stress-change distribution. This time-dependent fault slip is enforced as a displacement discontinuity along the prescribed fault interface of the tetrahedral mesh. This dynamic relaxation simulation is run for 99 seconds, allowing all seismic waves to exit the computational domain.

Text S8. Structural model, adaptive meshing and resolution

We construct a structural model that incorporates GEBCO-derived topography and bathymetry at 900 m resolution. This free surface is intersected by a smoothed curved fault geometry, derived from the geometry of the geodetic slip model. The fault is embedded within the same 1D velocity model as used in the geodetic inversion. The computational domain spans $630 \times 900 \times 200\ \ \mathrm{km}^3$.

For the ensemble rupture models, we employ a non-uniform unstructured tetrahedral mesh comprising approximately 4 million elements. Along the Sagaing Fault, this mesh resolves fault geometry with 700 m element size, while surface topography and bathymetry are represented at 2 km resolution. A refined mesh region measuring $80 \times 500 \times 40$ km^3, centered on the fault, uses element sizes of 2 km. Outside this region, the mesh is progressively coarsened up to a maximum element size of 15 km. We use high-order polynomials of degree $p = 4$, enabling sub-element resolution in space and high-order accuracy in time. Simulating 130 s of rupture dynamics and seismic wave propagation requires 350 CPU hours on the Skylake-based SuperMUC-NG Phase 2 supercomputer at the Leibniz Supercomputing Center, Garching, Germany. The total computational cost of the 180 model ensemble is therefore only ∼60k CPUh.

The on-fault resolution is chosen to resolve the process zone width[51], the region behind the rupture front where shear stress drops, controlled by fault friction and stress parameters ([52], Table S2). In our preferred dynamic rupture model, the median process zone width is ≈ 1960 m, with 95% of ruptured fault elements exceeding 625 m in size. SeisSol simulations with $p = 4$ require at least 2-3 elements across the median process zone for adequate resolution[53]. With a fault element size of h =700 m and 25 quadrature points per cell, our simulations meet this requirement, ensuring accurate resolution of the dynamic rupture process.

Text S9. Dynamic rupture model frictional strength, stress drop and nucleation

We prescribe a constant dynamic friction coefficient, enforce a minimum friction drop of $\mu_\mathrm{s} - \mu_\mathrm{d} \geq 0.2$, and introduce spatial variations in static friction μ_s, thereby adopting heterogeneous initial shear stress (τ_gsm) while maintaining a constant relative prestress ratio R in regions where $\mu_\mathrm{s} > 0.35$.

R is a key dynamic rupture parameter (e.g. [54]), and is critical in determining rupture style and speed (e.g.,[55]) and relates the potential maximum stress drop $\tau_0 - \tau_\mathrm{d}$, with τ_0 the initial shear stress and τ_d the dynamic shear stress, to the frictional strength drop $\tau_\mathrm{s} - \tau_\mathrm{d}$, with τ_s the static shear stress, as

$$R = (\tau_0 - \tau_\mathrm{d})/(\tau_\mathrm{s} - \tau_\mathrm{d})\,, \tag{5}$$

with τ_s the static fault strength defined as

$$\tau_\mathrm{s} = \mu_\mathrm{s}\sigma'_\mathrm{n}\,, \tag{6}$$

and τ_d is the dynamic fault strength defined as

$$\tau_\mathrm{d} = \mu_\mathrm{d}\sigma'_\mathrm{n}\,, \tag{7}$$

with σ'_n the effective normal stress.

We assume an effective normal stress that increases linearly from 1 MPa at the surface to 16 MPa at 1.5 km depth, and remains constant below this depth. Such low effective normal stress is motivated by the modest stress changes implied by the inferred slip distribution and are consistent with pore-fluid overpressure observations at interplate boundaries, following the lithostatic gradient below a critical depth[56]:

$$\sigma'_\mathrm{n} = \min(-1 \times 10^6, \max(-16 \times 10^6, 0.4\rho g z))\,. \tag{8}$$

Here, σ'_n is negative in compression. The sharp near-surface gradient of $|\sigma'_\mathrm{n}|$ is required to allow sufficient potential stress drop at shallow depth and to capture the large shallow slip observed near the surface.

Assuming simple friction parameter distributions in conjunction with a heterogeneous initial stress derived from the geodetic slip distribution provides a simple and parsimonious way of setting up initial conditions for dynamic rupture models. However, this strategy is often inefficient in practice: the stress field inferred from the slip distribution is typically too heterogeneous, and regions of low slip then tend to remain insufficiently critically stressed[47]. Therefore, many previous studies constraining dynamic rupture models from slip distributions[29;47;57] introduce small-scale spatial variations in static or dynamic friction, reflecting the heterogeneous shear stress (here τ_gsm), thereby effectively enforcing a constant R across the entire fault. However, there is no clear physical basis for prescribing static and dynamic friction coefficients as functions of a heterogeneous initial shear stress distribution.

Here, we enforce a constant $R = R_\mathrm{param}$ in region of sufficient large intial stress (resulting in $\mu_\mathrm{s} \geq 0.35$), while enforcing a relatively large minimum friction drop ($\mu_\mathrm{s} - \mu_\mathrm{d} \geq 0.2$) so that low-intial-stress regions are not unrealistically close to failure. This strategy leads to a heterogeneous relative prestress ratio R distribution, with $R < R_\mathrm{param}$ in low initial-stress regions and $R = R_\mathrm{param}$ elsewhere (Figure S24e.).

Figs. S25 and S24 illustrate how spatial variations in initial stress and friction parameters affect shear stress and fault strength, shown for three representative depth profiles and for their distribution in the preferred dynamic rupture model.

In all models, we prescribe the same nucleation patch that grows smoothly in time and across a minimal-sized perturbation area[58], adapted to the respective friction and stress parameters. The center of this patch is placed at the USGS inferred hypocenter location (22.011°N 95.936°W, 7.6 km depth)[59].

Text S10. Dynamic rupture ensemble parameter space

To generate an ensemble of 180 dynamic rupture simulations systematically exploring unconstrained dynamic parameters, we vary only three fault-wide defined quantities: (i) C, scaling the critical slip-weakening distance d_c in the linear slip-weakening friction law, (ii) B, modulating the potential maximum stress drop proportionally to the shear stress changes derived from the geodetic slip model, and (iii) R_{param}, the prescribed relative prestress ratio (Equation 5) in region where $\mu_s > 0.35$. We explore all combinations of $(B, C, R_{\mathrm{param}})$ with B in $[0.9, 0.95, 1.0]$, C in $[0.05, 0.1, 0.15, 0.2, 0.25, 0.3]$, and R in $[0.5, 0.55, 0.6, 0.65, 0.7, 0.75, 0.8, 0.85, 0.9, 0.95]$, leading to $3 \times 6 \times 10 = 180$ models.

The critical slip-weakening distance d_{c} is defined proportional to the slip distribution of the geodetic slip model u_{gsm} (Fig. S24a) as

$$d_{\mathrm{c}} = C \max\big(0.15 \max(u_{\mathrm{gsm}}),\, u_{\mathrm{gsm}}\big)\,. \tag{9}$$

This proportionality is tapered to 15% of the maximum slip, limiting computational cost and prevents unrealistically low fracture energy and dynamic rupture propagation far into low-slip regions.

A slip-scaled d_{c} assumption [29;57] produces scale-dependent fracture energy [52;60] with fault slip, as proposed by [61;62]). This promotes dynamic rupture propagation in regions of low slip while using larger d_{c} in where slip is high, which is consistent with near-source seismic observation during large earthquakes [63] and Bayesian dynamic rupture inversion [64;65].

The initial fault traction vector $\boldsymbol{\tau}_0$ is set as

$$\boldsymbol{\tau}_0 = B\boldsymbol{\tau}_{\mathrm{gsm}} + \boldsymbol{\tau}_{\mathrm{d}}\,, \tag{10}$$

where $\boldsymbol{\tau}_{\mathrm{gsm}}$ is the shear stress change vector from the geodetic slip model, and $\boldsymbol{\tau}_{\mathrm{d}}$ is the dynamic strength vector defined as:

$$\boldsymbol{\tau}_{\mathrm{d}} = \mu_{\mathrm{d}} \sigma'_{\mathrm{n}} \boldsymbol{u}_{180}\,, \tag{11}$$

with $\boldsymbol{u}_{180}$ a unit vector pointing in the rake 180° direction, and σ'_{n} the effective normal stress.

This formulation ensures that the potential stress drop $\tau_0 - \tau_{\mathrm{d}}$ equals τ_{gsm}. This allows the dynamic rupture models to accurately and spontaneously reproduce the geodetic slip distribution (see Fig. S23).

Our back-projection analysis (Figure 4 in the main text) indicates that the fault region north of the hypocenter ruptured at subshear velocity, which can only be reproduced with sufficiently high local fracture energy. We therefore modify the parameterization north of the hypocenter by reducing the relative prestress ratio to $R_{\mathrm{north}} = \min(0.6, R_{\mathrm{param}})$ and increasing the fracture energy coefficient to $C_{\mathrm{north}} = \max(0.25, C)$. We find a single fault-wide parametrization cannot simultaneously capture both the subshear rupture to the north and the supershear rupture rapidly accelerating toward P-wave velocity in the south.

The preferred dynamic rupture model is obtained with $B = 0.95$, $C = 0.15$, and $R = 0.95$ (see Table S2). $B = 0.95$ corresponds to a slightly reduced prestress level relative to that directly inferred from the geodetic slip model. With $C = 0.15$, the resulting d_{c} ranges from 0.12 m to 0.82 m, lower than estimates of 1.2 m from on-fault inferences at the CCTV site [66] and 2.4 m from analysis of parallel velocity pulses in strong-motion records at the near-fault NPW station [66] using the method of Fukuyama and Mikumo (2007) [67]. Finally, $R_{\mathrm{param}} = 0.95$ corresponds to a near-critical fault stress state. The preferred dynamic rupture model is characterized by a very low fracture energy $G_{\mathrm{c}} = 8 \times 10^5$ J/m^2), compared to estimates from previous 3D earthquake rupture scenarios (Table S1 in [62]). Figure S24 illustrates the spatial distribution of fault friction, slip-weakening distance, shear and normal stress, and relative prestress ratio R of the preferred dynamic rupture model.

Text S11. Goodness of fit and preferred dynamic rupture model validation

We identify a preferred model from the ensemble of dynamic rupture scenarios by ranking all 180 simulations according to a weighted, combined goodness-of-fit metric, denoted as $\mathrm{GOF}_{\mathrm{combined}}$. This metric integrates multiple individual goodness-of-fit (GOF) measures, each reflecting a distinct evaluation criterion.

The combined score is defined as

$$\mathrm{GOF}_{\mathrm{combined}} = \sum_i w_i \mathrm{GOF}_i \,, \tag{12}$$

where GOF_i is the GOF value for criterion i and w_i is the corresponding weight.

Specifically, we combine constraints from (i) the slip distribution of the geodetic model, (ii) the NS displacement component at near-fault seismic static NPW, (iii) slip-rate inferred from the CCTV observations, (iv) surface fault-offsets, (v) the moment-rate function of the USGS finite-fault model, and (vi) fits to teleseismic surface and body waveforms. A short description of each component and its associated weight is given in Table S3.

To emphasize the most diagnostic constraints on rupture dynamics, we assign higher weights to the near-fault NPW and CCTV record, the geodetic slip distribution and fault offsets, compared to teleseismic inferences (e.g.,[68]). The preferred model has a GOF of 0.71, and the ensemble shows a large spread in GoF (Fig. S26).

Validation of the preferred dynamic rupture model is illustrated in Figure 4 of the main text. Modeled fault-parallel surface offsets are consistent with Sentinel-2 optical image cross-correlation. The moment-rate function of the preferred model shows an early high-amplitude peak associated with the bilateral phase, followed by a prolonged tail from unilateral supershear propagation, and compares well with the USGS kinematic model[69], the SCARDEC source time function[70], and an alternative kinematic model[71]. Ground displacement at near-fault station NPW[72] matches the modeled displacement, with the observed series derived by double integration and detrending of accelerations and subject to an estimated ±0.8 s timing uncertainty. Along-strike slip-rate inferred from CCTV footage[73], recorded 124 km south of the epicenter, is also reproduced in both shape and peak amplitude, with absolute timing aligned based on onset time using a slip-rate threshold of 0.15 m/s. Back-projection results from seismic arrays in Australia, Europe, and Alaska (Figs. 4e,f and S34) are consistent with the modeled rupture front, with marker size representing normalized beam energy and color denoting rupture time. Finally, rupture speeds inferred from back projection align with those of the preferred model, with the model's median rupture onset time and depth-dependent spread reproducing the observed along-strike evolution.

Text S12. Variability within the dynamic rupture model ensemble

We analyze the ensemble of 180 dynamic rupture simulations, synthesized in Figures S27, S28, and S29. Each figure illustrates model variability with varying critical slip weakening distance (via C) and relative prestress ratio (R_{param}), while keeping B fixed. Most models rupture the full fault extent as defined by the geodetic slip model, producing a moment magnitude near M_w 7.8. Rupture duration, however, varies widely, ranging from 81 s to 148 s. The fastest models nucleate early and propagate nearly continuously at supershear rupture speeds approaching the local P-wave velocity, whereas slower models alternate between sub-shear and supershear propagation (Fig. S30). The unique near-fault observations of the Myanmar earthquake clearly distinguish between these variable rupture speeds.

The surface-averaged fracture energy G_{c} (Figure S27c) helps explain this variability. It is calculated as

$$G_{\mathrm{c}} = \frac{1}{2}(\mu_{\mathrm{s}} - \mu_{\mathrm{f}}) \min(u, d_{\mathrm{c}}) \sigma'_{\mathrm{n}} \,, \tag{13}$$

where u is the accumulated fault slip and μ_f is the local friction coefficient at the end of the simulation. G_c decreases with smaller C and larger R. Models with similar G_c tend to produce comparable rupture durations and moment magnitudes, although variability in moment magnitude is generally smaller.

Figure S31 shows the variation of individual goodness-of-fit (GOF, Text S11, Table S3) components with C and R at fixed $B = 0.95$, which yields the highest combined GOF. Distinct trade-offs emerge, highlighting the challenge of finding a dynamic rupture model compatible with all observables: models that best reproduce the NS displacement waveform at NPW favor short durations (82–83 s), low C (0.05), and moderate closeness to failure R (0.75). In contrast, the CCTV-inferred slip-rate[73] favors larger $C = 0.2$ and higher relative prestress ($R > 0.75$). However, in the regime where the fault slip distribution is well reproduced (GOF > 0.90), the CCTV slip-rate GOF is nearly insensitive to the prestress ratio R. This indicates that C, and thus the slip weakening distance d_c, primarily controls the shape of the on-fault slip-rate pulse. Models that optimize fit to the teleseismic body waveforms require even larger C (0.3). Fitting the geodetic slip distribution, the USGS moment rate function, and teleseismic surface waves (Figures S31c,f,g) excludes longer-duration models (>110 s) dominated by subshear rupture phases. However, these observables do not strongly discriminate among shorter-duration models. This is consistent with Figure S27e, where we show that several short-duration models reproduce the inferred USGS moment rate function. The GOF distributions of teleseismic body and surface waveforms (Fig. S31d,g) are complex and contradictory, providing limited guidance for identifying favorable models. We therefore assign these observables a lower weight in our combined GOF definition.

Text S13. Back-projection

Teleseismic back projection[74] is widely used to image the rupture process of large earthquakes and to estimate rupture speed. Here, we apply a time-domain, phase-weighted, relative back-projection technique[75] to track the rupture of the 2025 Mandalay earthquake. This variation of back-projection has been shown to enhance correlated signals.

We use data from three regional arrays in Alaska, Australia, and Europe, and perform back projection for each array independently (Fig. S34). Stations with epicentral distances between 40° and 90° are considered, followed by several preprocessing steps. All waveforms are band-pass filtered between 0.4 and 2 Hz using a fourth-order Butterworth filter. One station with a high signal-to-noise ratio (SNR) is chosen as the reference for each array. SNR is calculated as the ratio of the mean-squared amplitude within a 1-s window containing the beginning of the P wave to that of the 10-s window immediately preceding the P-wave onset. Station AK.BARN (SNR = 2.2) is selected for Alaska, 2O.BTL02 (SNR = 2.6) for Australia, and BW.FFB1 (SNR = 2.3) for Europe. For each region, we extract a 10-s window that begins 4 s before the P arrival at the reference station. We slide this window along every other station's trace near the expected P-wave onset, compute the cross-correlation at each lag, and keep the lag that yields the maximum coefficient. Stations whose peak coefficient exceeds an empirically determined threshold (Alaska > 0.7; Australia > 0.85; Europe > 0.8) are retained, and each accepted trace is shifted by the lag of its peak to align the P-wave onsets. These thresholds were chosen empirically to account for regional differences in data quality. To maintain uniform station spacing, any station within 0.5° of a selected station is discarded. The final arrays comprise 81 stations in Alaska, 62 in Australia, and 31 in Europe.

Given the fault's simple, subvertical geometry, we restrict candidate rupture nodes to be beneath the mapped surface trace. This method has been applied in previous studies[48]. The surface trace, derived from Sentinel-2 optical offsets, is resampled onto a grid with 1 km spacing. We assume the hypocenter to be 22.012153°N, 95.982254°E and 7.6 km deep, which is the closest fault trace node from the USGS epicenter[59]. Travel times from each grid node to every station are computed with the global IASP91 one-dimensional velocity model[76]. Waveforms are then stacked in a 10-s moving window with 1-s increments. At each step we identify the grid node with the highest stacked energy as the preliminary subevent, continuing this procedure until 110 s after the origin time. Only subevents whose energy exceeds 2% of the overall maximum are retained in the final rupture model.

Supplementary Animation

We provide an animation illustrating the preferred dynamic models at https://syncandshare.lrz.de/getlink/fi6jJWvERN2pajq6kaxqHk/.

Animation S1 (Preferred_dynamic_rupture_model_Myanmar.mp4): Rupture evolution in the preferred dynamic model, shown as absolute slip rate (m/s).

Satellite	Track	Orbit	Acquisition dates	$B_\perp$ (m)
ALOS-2	152	ascending	2025/02/11 – 2025/04/08	179
ALOS-2	41	descending	2025/01/09 – 2025/03/30	305
ALOS-2	42	descending	2025/02/21 – 2025/05/02	6
Sentinel-1A	33	descending	2025/03/19 – 2025/03/31	103
Sentinel-1A	106	descending	2025/03/24 – 2025/04/05	160
Sentinel-1A	70	ascending	2025/03/22 – 2025/04/03	18
Sentinel-1A	143	ascending	2025/03/24 – 2025/04/05	23

Table S1: SAR data used in this study. $B_\perp$ is a perpendicular baseline between the respective repeat orbits.

Parameter	Symbol	Range	Preferred Value
Static friction coefficient	μ_s	0.35–0.65	
Dynamic friction coefficient	μ_d	0.15	
Critical slip weakening distance	d_c	proportional to slip ($\times\mathcal{C}$)	
Cohesion	c	0.25–1.25 MPa	
Effective normal stress	$\lvert\sigma'_\mathrm{n}\rvert$	1–16 MPa	
Heterogeneity strength scaling	$\mathcal{B}$	0.9 - 1.0	0.95
Fracture energy scaling	$\mathcal{C}$	0.05 - 0.3	0.15
Relative prestress ratio	$\mathcal{R}$	0.5 - 0.95	0.95

Table S2: Dynamic rupture model ensemble parameters assumed constant or varied within a certain range.

GOF component	**Weight**	**Description**
Slip distribution	1.5	GOF to the geodetic slip model (interpolated onto the same grid, and computed as $1 - \exp(\text{RMS})$)
Slip rate at CCTV	2.5	GOF to the inferred slip rate at the CCTV location (computed as $1 - \exp(\text{RMS})$), aligned using cross-correlation
Displacement waveform at NPW	2.0	GOF, computed as $1 - \exp(\text{RMS})$, to the NS component displacement waveform at station NPW, obtained by double integration
Fault offsets	1.5	GOF with Sentinel-2–derived fault offsets, computed as $1 - \exp(\text{RMS})$
Moment rate function	1.0	GOF from cross-correlation with the moment rate fuction of the USGS finite-fault model
Teleseismic body waveforms	1.0	GOF from cross-correlation (max shift = 2.5% of travel time) of observed and synthetic P and SH displacements, using a 170 s window (starting 20 s before arrival) and band-pass filtered to 20–150 s
Teleseismic surface waveforms	1.0	GOF from cross-correlation (max shift = 100 s) of observed and synthetic 3-component displacements, using a 3000 s window (from event onset) and band-pass filtered to 100–500 s

Table S3: Goodness-of-fit (GOF) components and associated weights used to select a preferred dynamic rupture model.

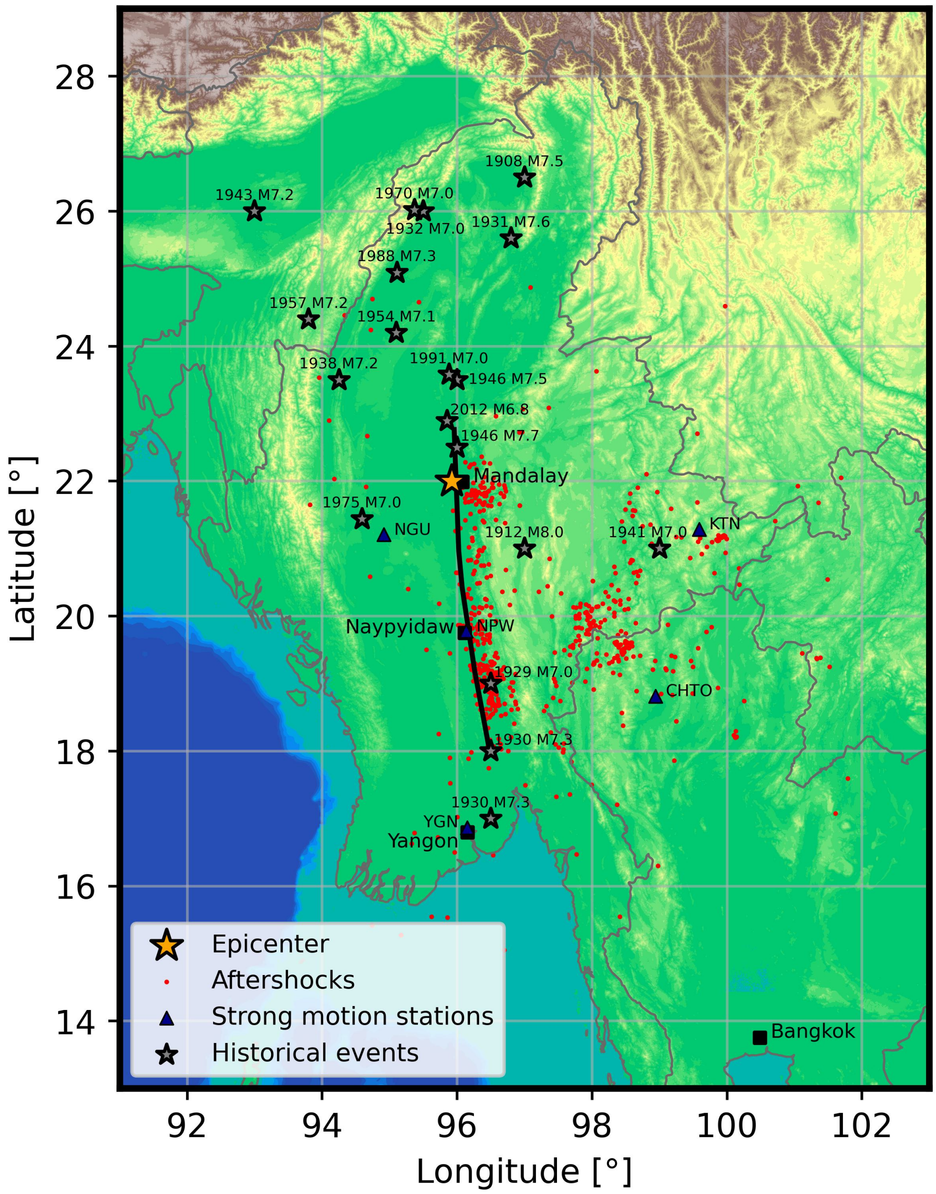

Fig. S1: Map of the study area. Colors represent topography. The solid black line marks the rupture trace of the 2025 Mandalay earthquake. Red dots show aftershock epicenters, black triangles mark strong-motion seismometer locations, and stars indicate epicenters of significant historical earthquakes [77].

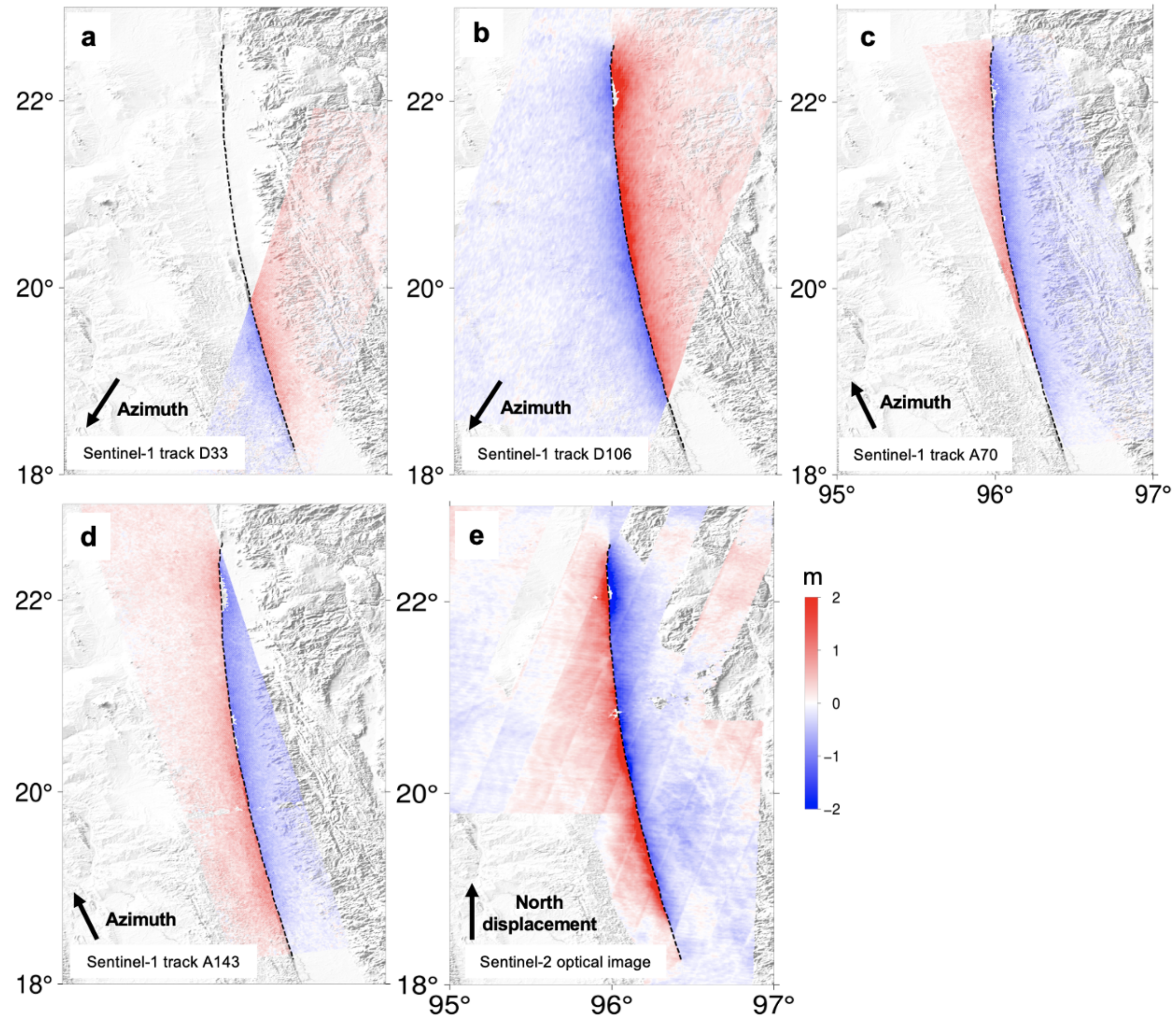

Fig. S2: (a-d) Azimuth offsets from Sentinel-1A SAR data (e) North-South offsets from Sentinel-2 optical image data. Arrows denote the direction on which the horizontal displacements are projected. Color denotes the displacement amplitude, in meters. Background shading denotes topography.

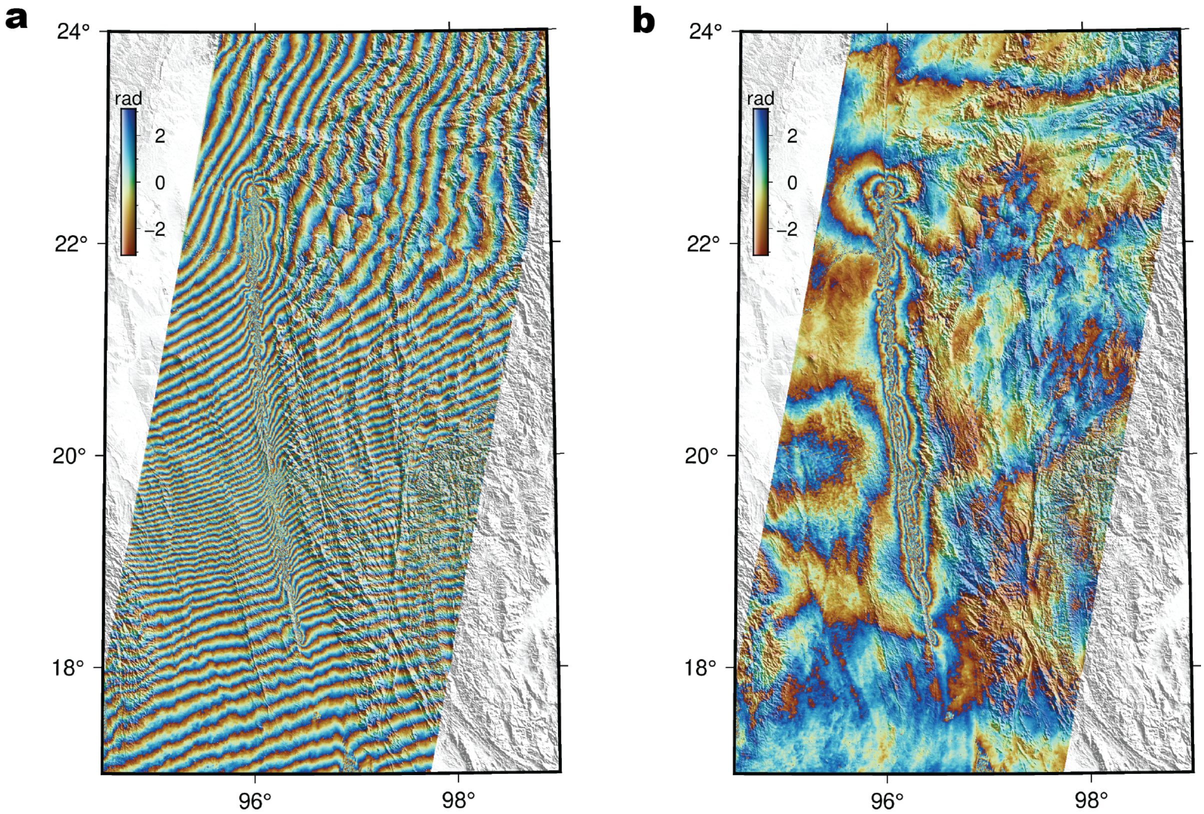

Fig. S3: (a) ALOS-2 interferogram from descending track 41. The interferogram is merged from 3 standard frames (3150, 3200, 3250) that were processed separately. (b) Same interferogram, after correcting for the long-wavelength trend. Each color fringe is equivalent to a displacement of 0.12 m in the satellite line of sight. Background shading denotes topography.

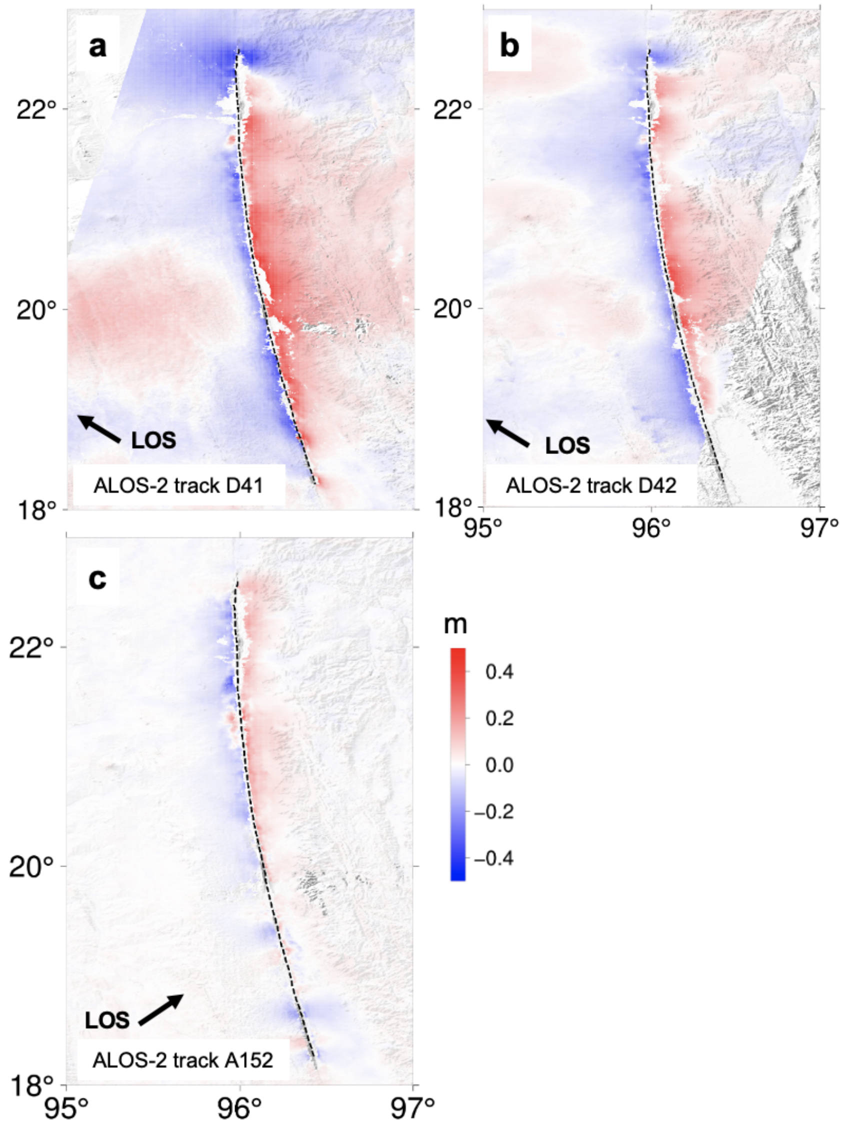

Fig. S4: Line of sight displacements (color), in meters, from ALOS-2 ScanSAR interferograms from 3 different satellite tracks. Motion toward the satellite is deemed positive. All maps cover the same area and have the same color range.

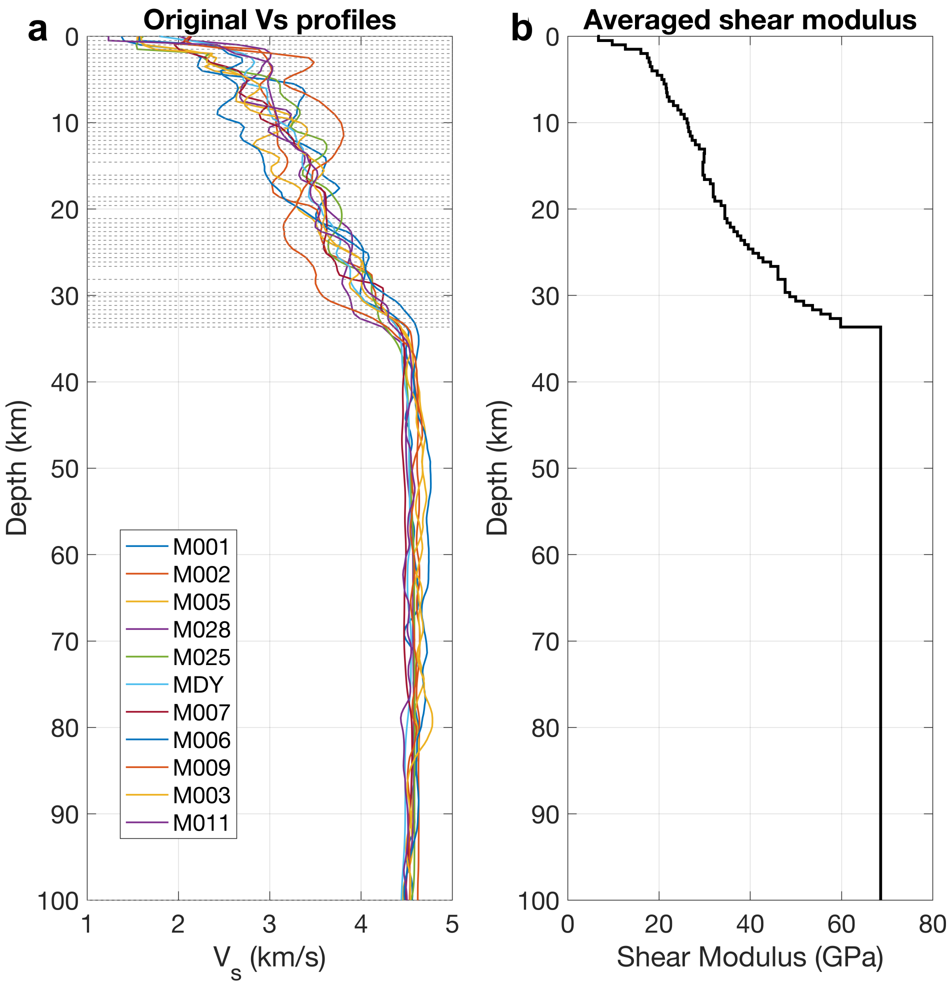

Fig. S5: Panel a: the 1-D shear wave velocity profile from the stations located within ~ 50 km from the Sagaing fault. The dashed lines indicate the bin boundaries. Panel b: the shear modulus calculated based on the depth-averaged shear wave velocity within each bin.

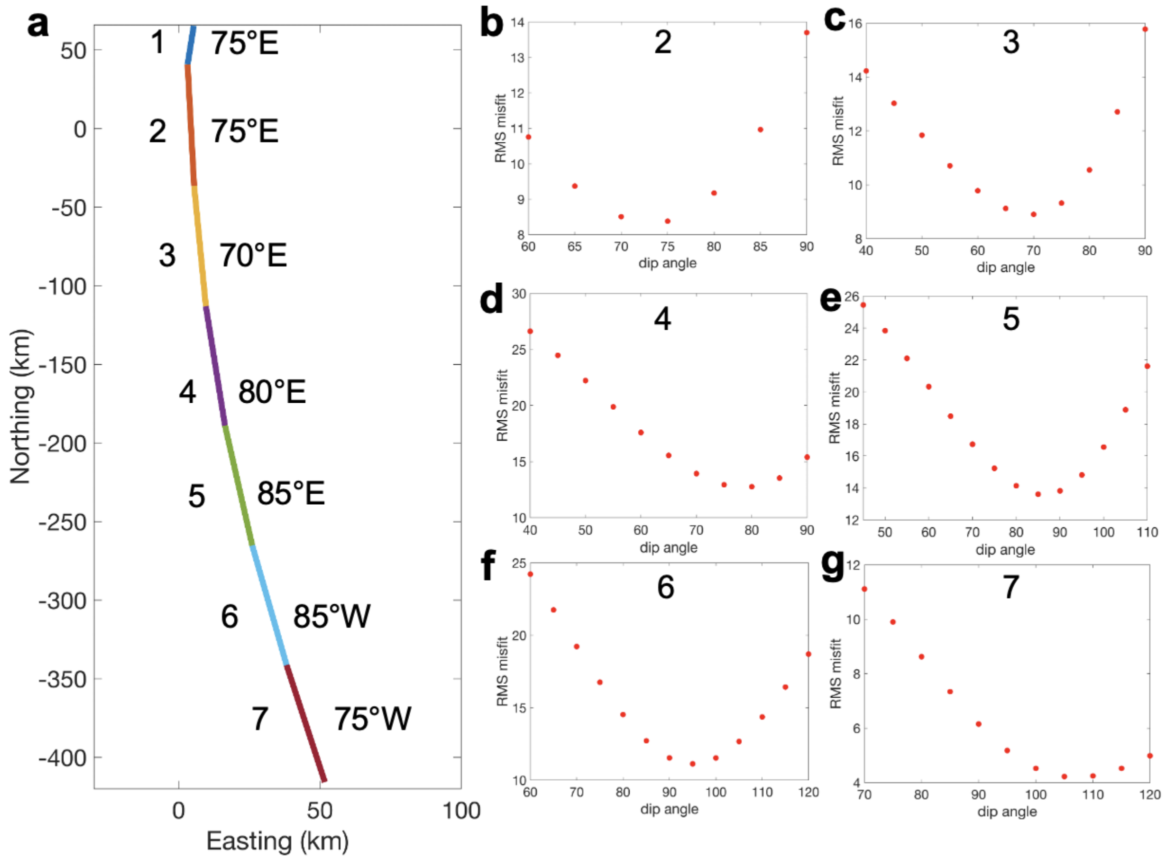

Fig. S6: Left panel: the segmented fault trace for the local dip angle estimation, plotted on UTM coordinates centered at (95.936°E, 22.011°N). Each segment is represented by a unique color and indexed by the number to the left. The preferred dip angle for each segment is marked to the right. Right panels: the dip angle vs RMS misfit test results for the determination of the preferred dip angle. The numbers on top represent the corresponding fault segment. The dip angle corresponding to Segment 1 is assumed to be the same as Segment 2.

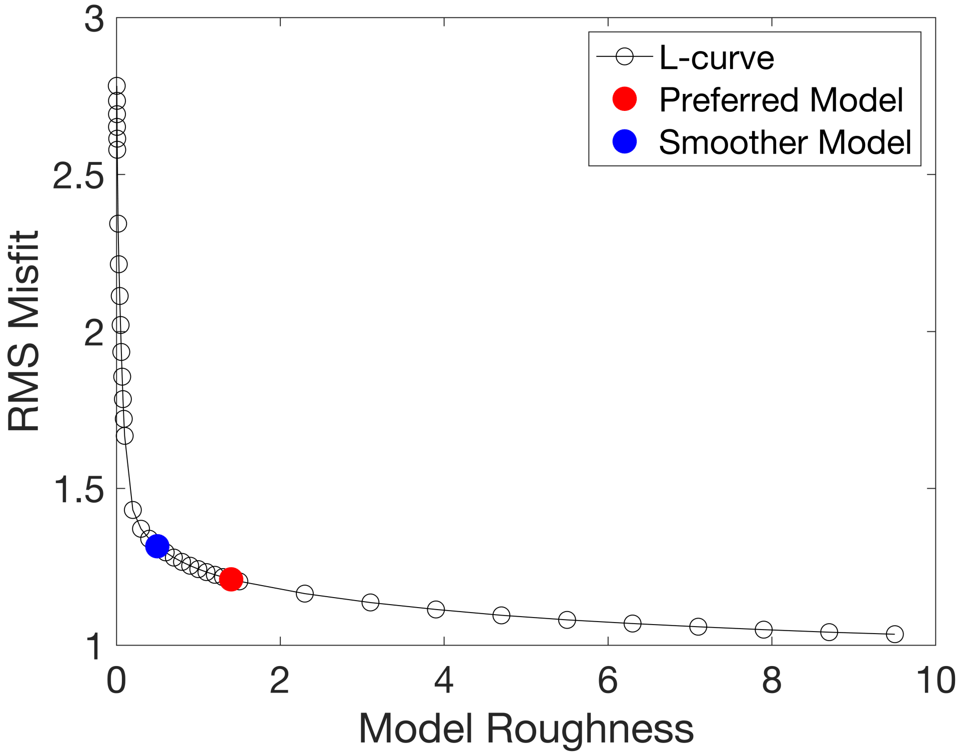

Fig. S7: The trade-off curve for selecting the preferred smoothness for the geodetic linear inversion. Red point: preferred model smoothness. Blue point: smoothness for a model with almost no shallow slip deficit without degrading significant data-model fitting (also see Fig S20.)

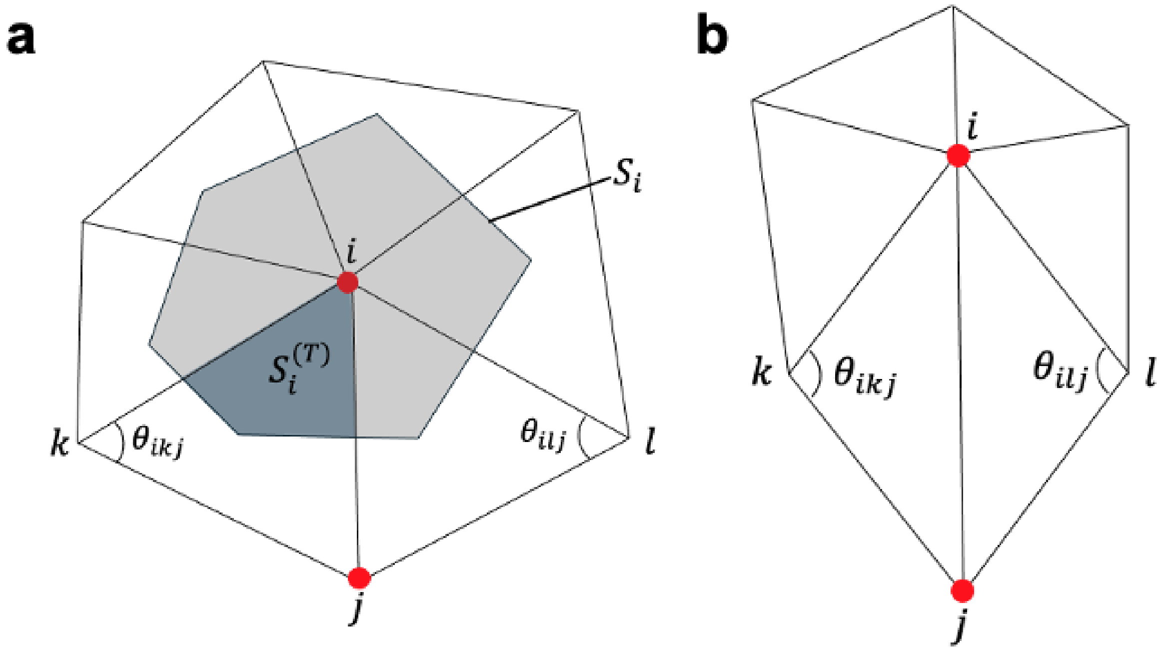

Fig. S8: Illustration of Laplacian weighting schemes for acute (panel a) and obtuse (panel b) triangles. S_i denotes the Voronoi cell area in the case when none of the triangles are obtuse. The dark-shaded area $S_i^{(T)}$ represents the Voronoi cell of an individual triangle ijk, part of the total Voronoi cell S_i of node i.

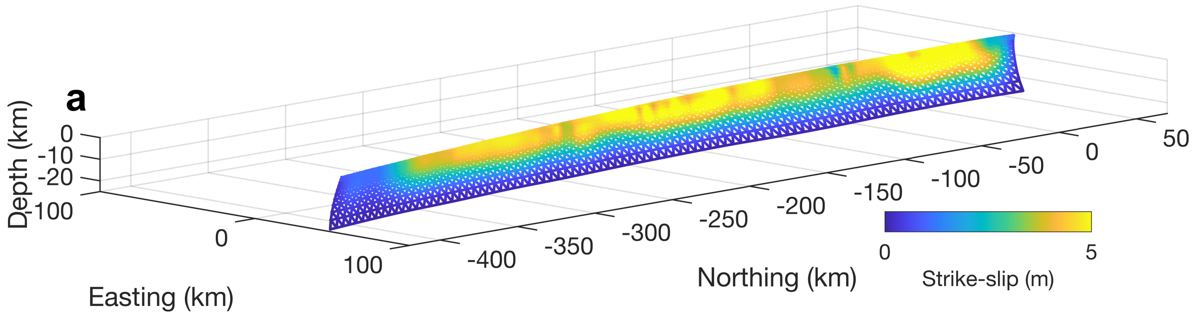

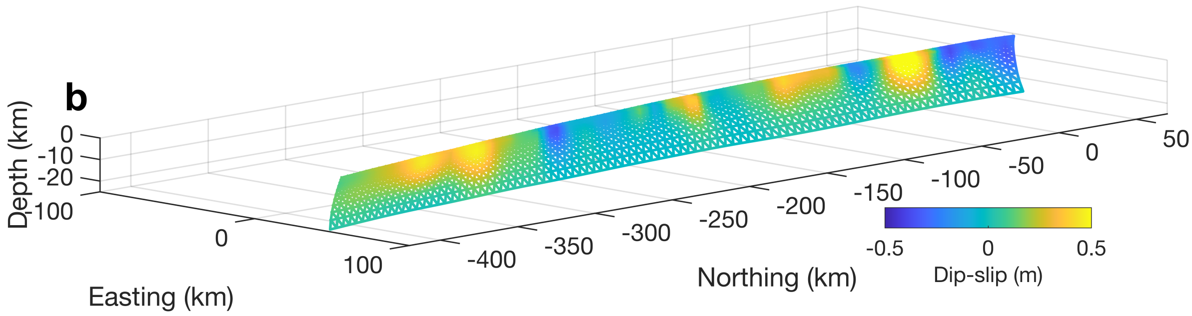

Fig. S9: The preferred static slip model from geodetic inversion assuming a curved rupture geometry with variable dip. Panel a: strike-slip; Panel b: dip-slip. Right-lateral strike slip and west-side-up dip slip are deemed positive.

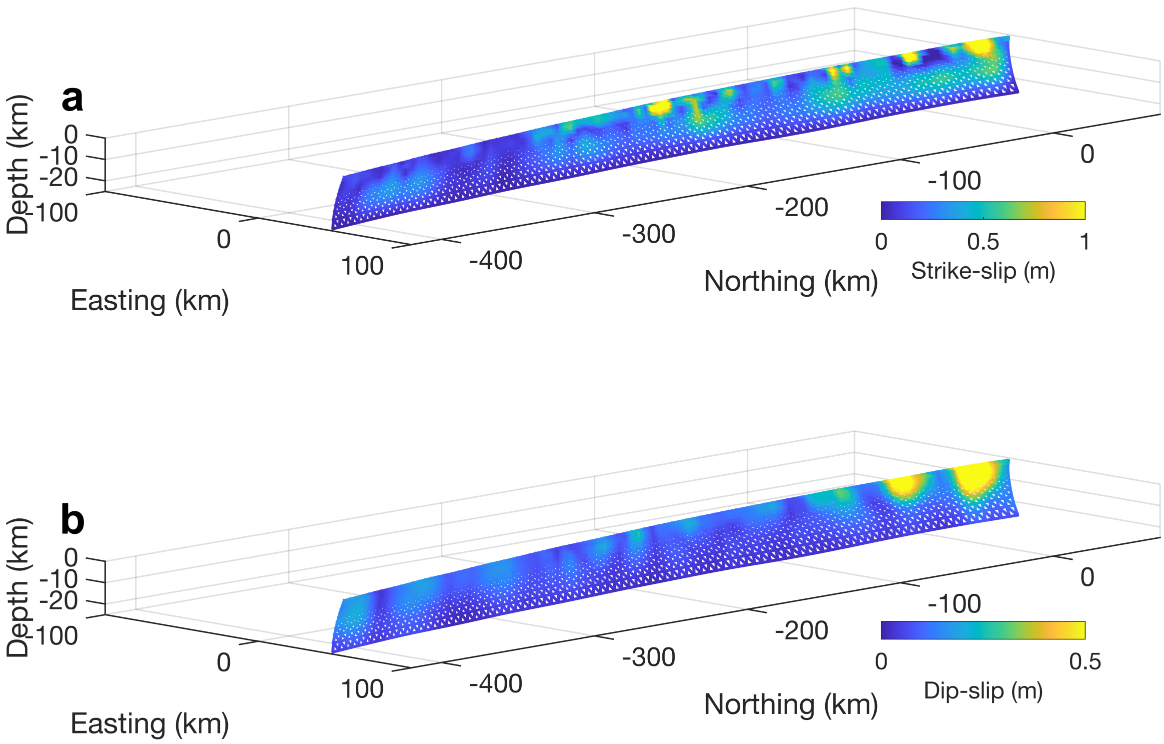

Fig. S10: The uncertainty of the static slip model computed using a bootstrap method. Panel a: strike-slip; Panel b: dip-slip.

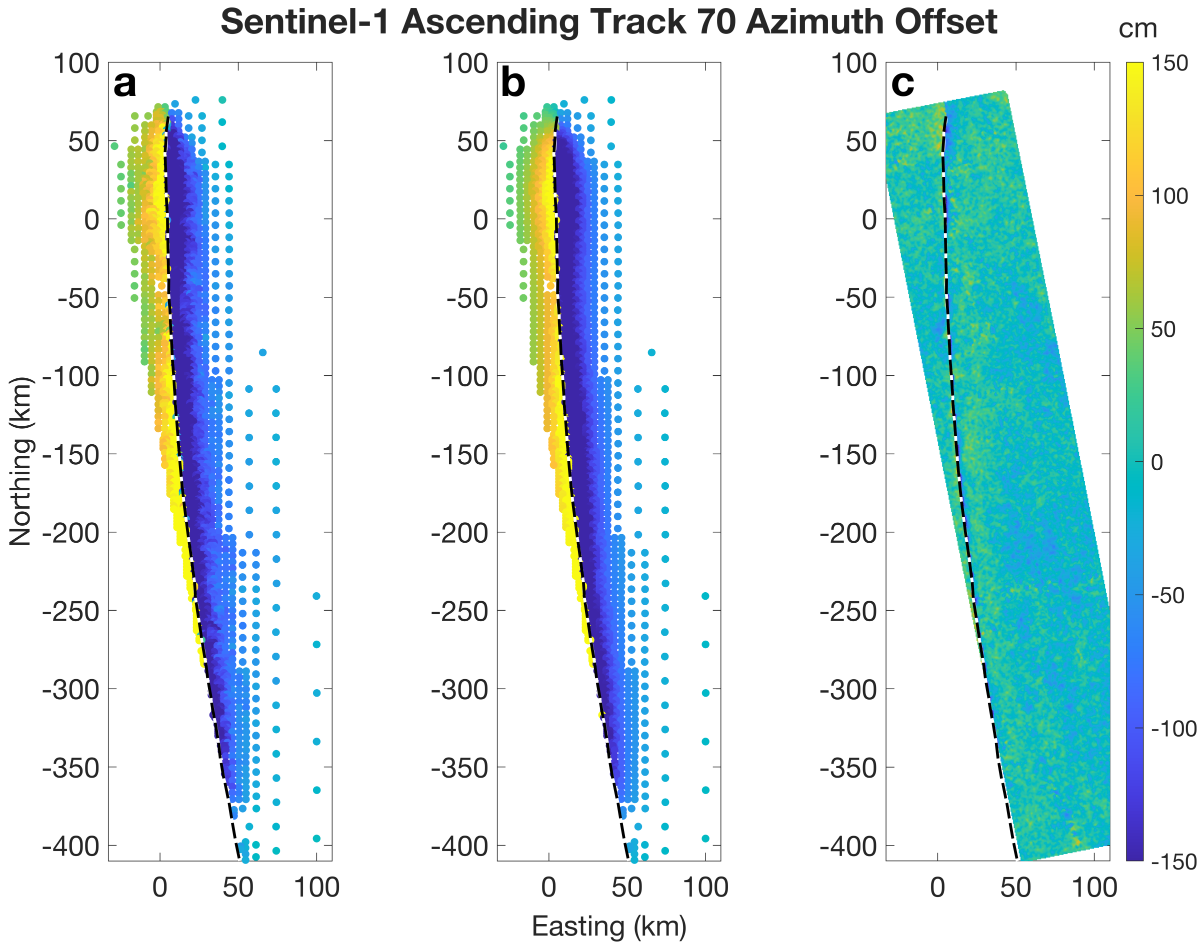

Fig. S11: (a) Sub-sampled data. (b) Best-fit model. (c) Residuals (difference between (a) and (b), evaluated at full resolution). The dashed line denotes the rupture trace.

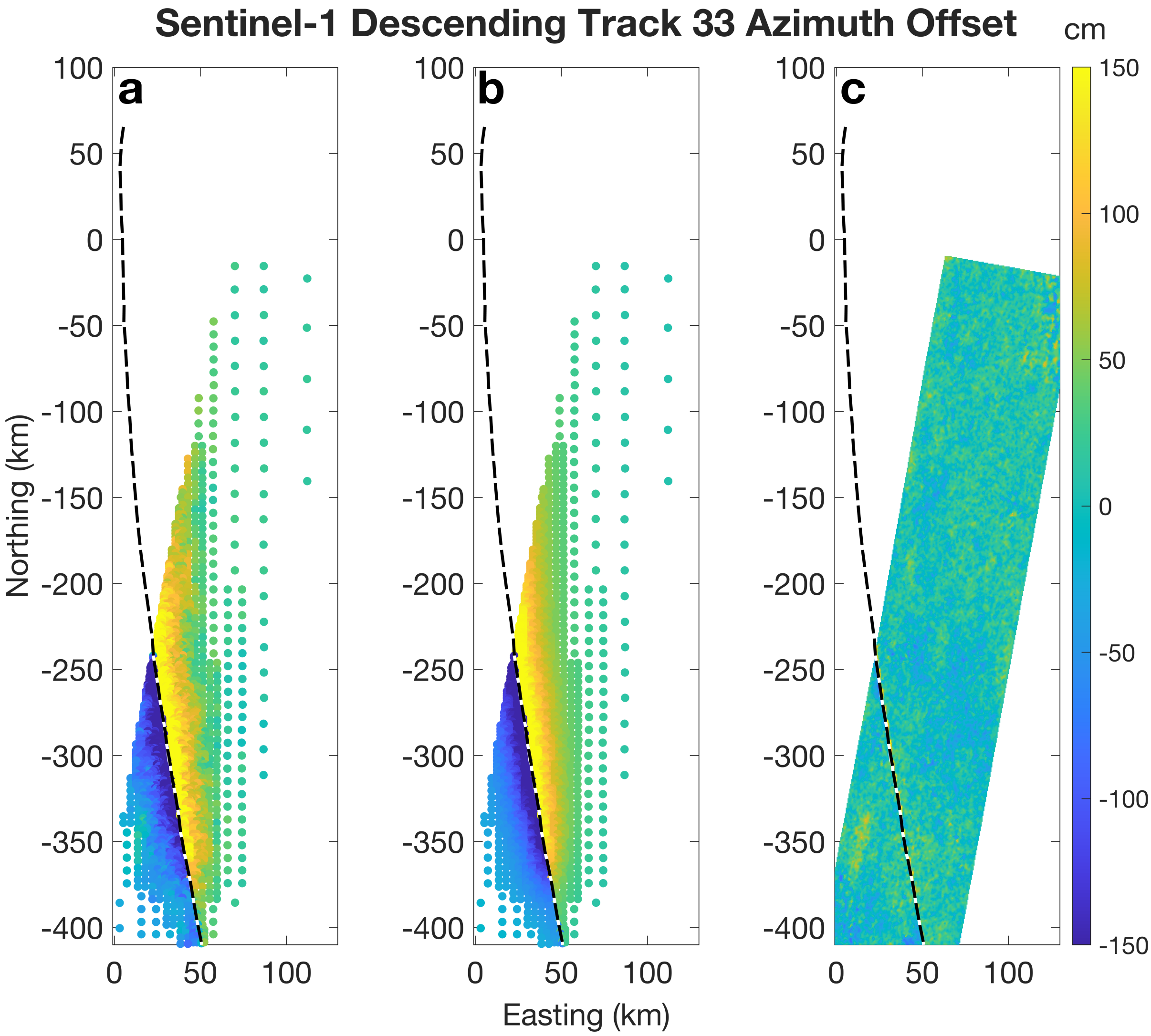

Fig. S12: (a) Sub-sampled data. (b) Best-fit model. (c) Residuals (difference between (a) and (b), evaluated at full resolution). The dashed line denotes the rupture trace.

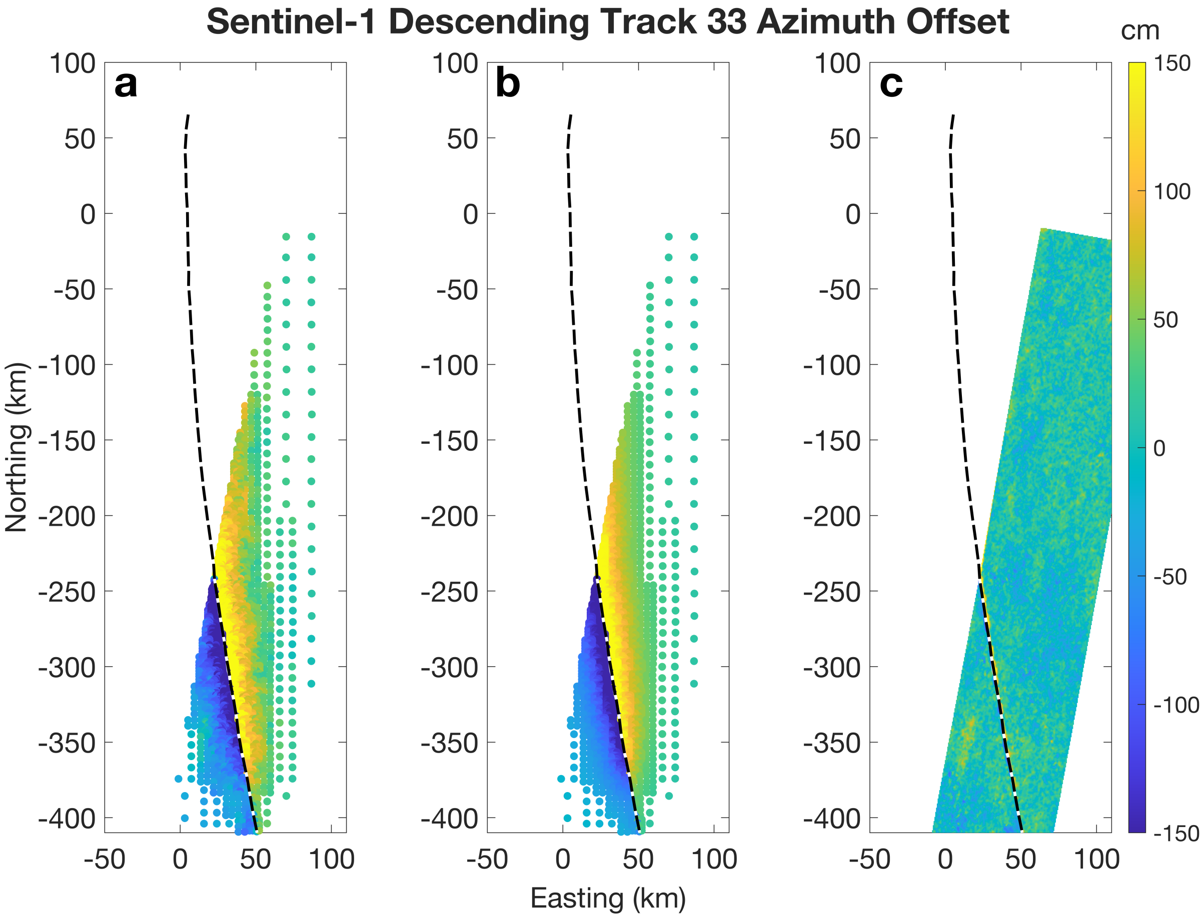

Fig. S13: (a) Sub-sampled data. (b) Best-fit model. (c) Residuals (difference between (a) and (b), evaluated at full resolution). The dashed line denotes the rupture trace.

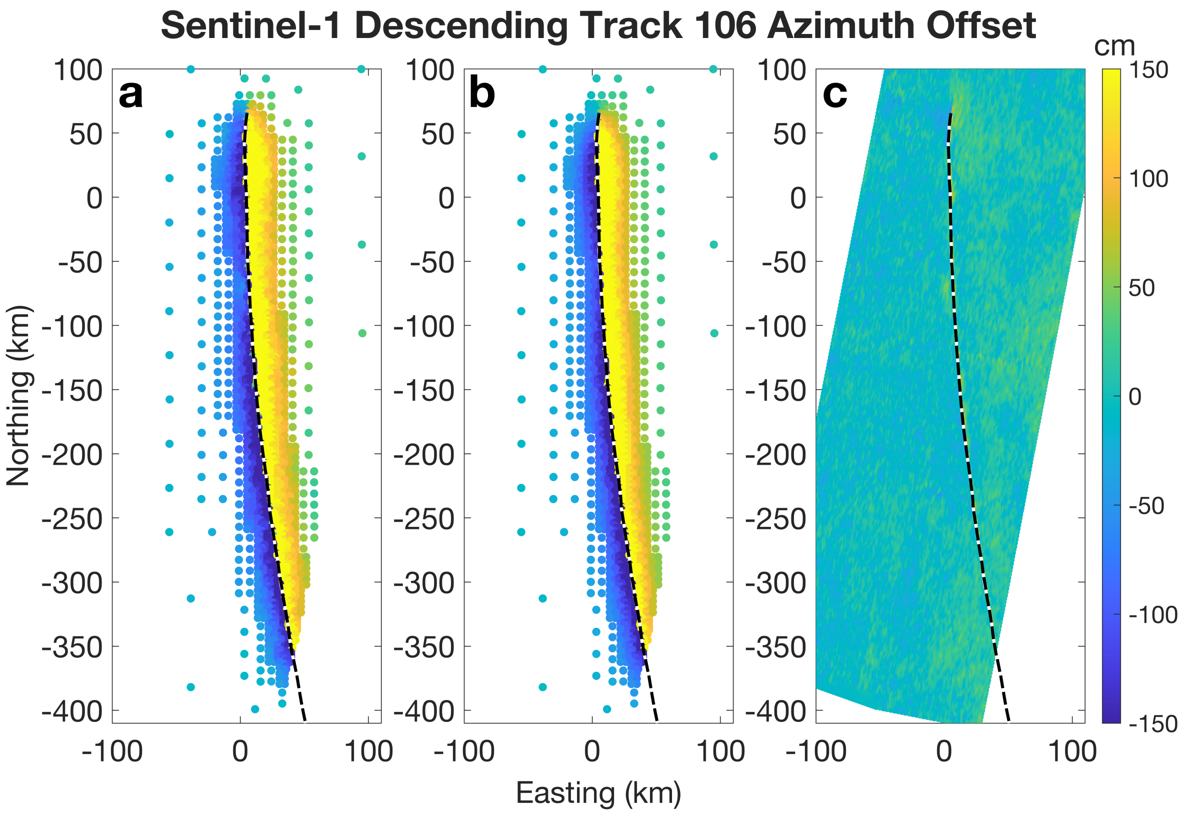

Fig. S14: (a) Sub-sampled data. (b) Best-fit model. (c) Residuals (difference between (a) and (b), evaluated at full resolution). The dashed line denotes the rupture trace.

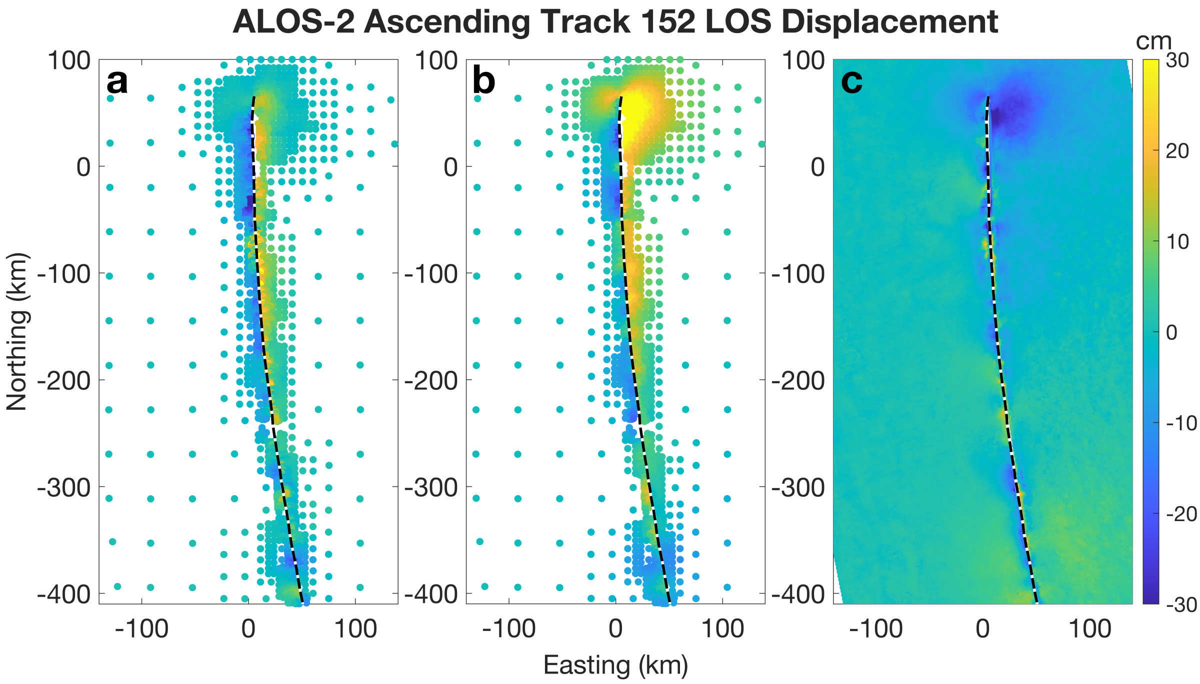

Fig. S15: (a) Sub-sampled data. (b) Best-fit model. (c) Residuals (difference between (a) and (b), evaluated at full resolution). The dashed line denotes the rupture trace.

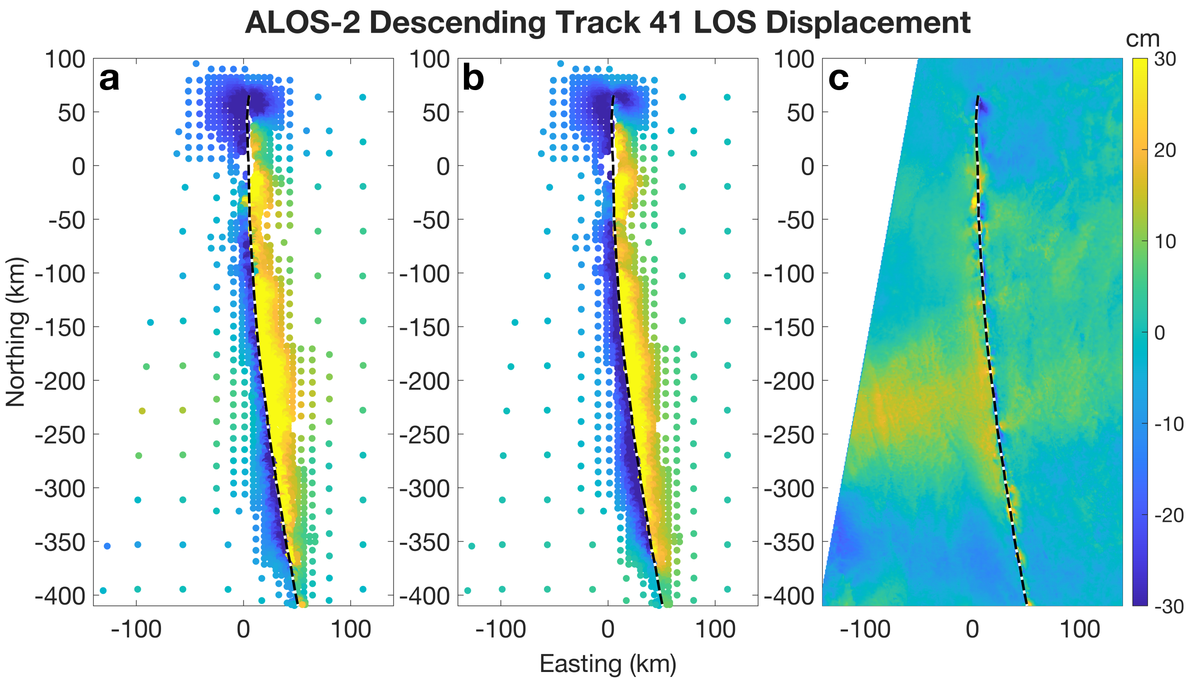

Fig. S16: (a) Sub-sampled data. (b) Best-fit model. (c) Residuals (difference between (a) and (b), evaluated at full resolution). The dashed line denotes the rupture trace.

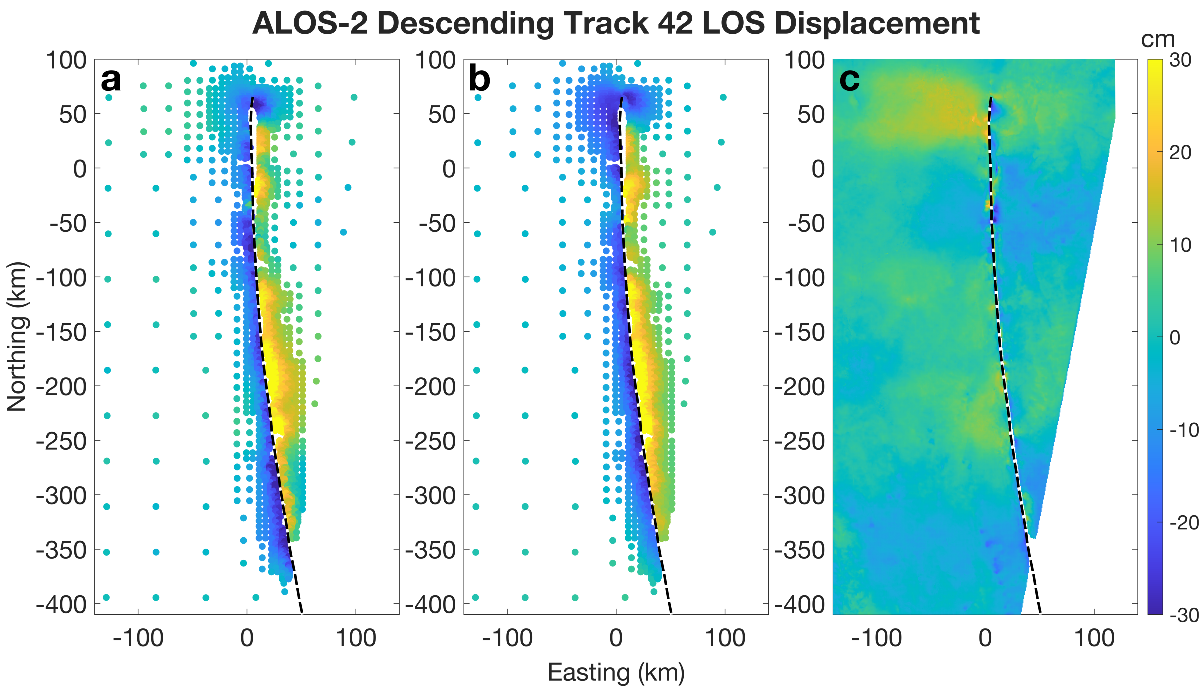

Fig. S17: (a) Sub-sampled data. (b) Best-fit model. (c) Residuals (difference between (a) and (b), evaluated at full resolution). The dashed line denotes the rupture trace.

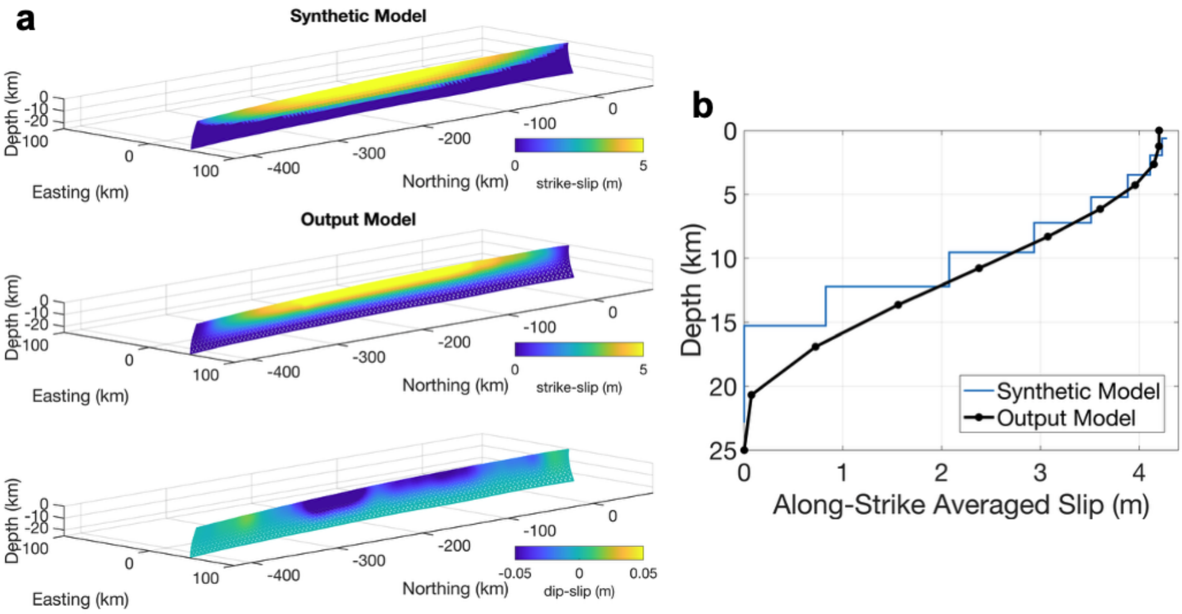

Fig. S18: Panel a, top: synthetic TDE model (strike-slip only) for resolution test; bottom: recovered slip from inversion of synthetic data and added noise, for strike-slip and dip-slip components. Right-lateral strike slip and west-side-up dip slip are deemed positive. Panel b: the along-strike averaged slip profile for the input model and inverse model.

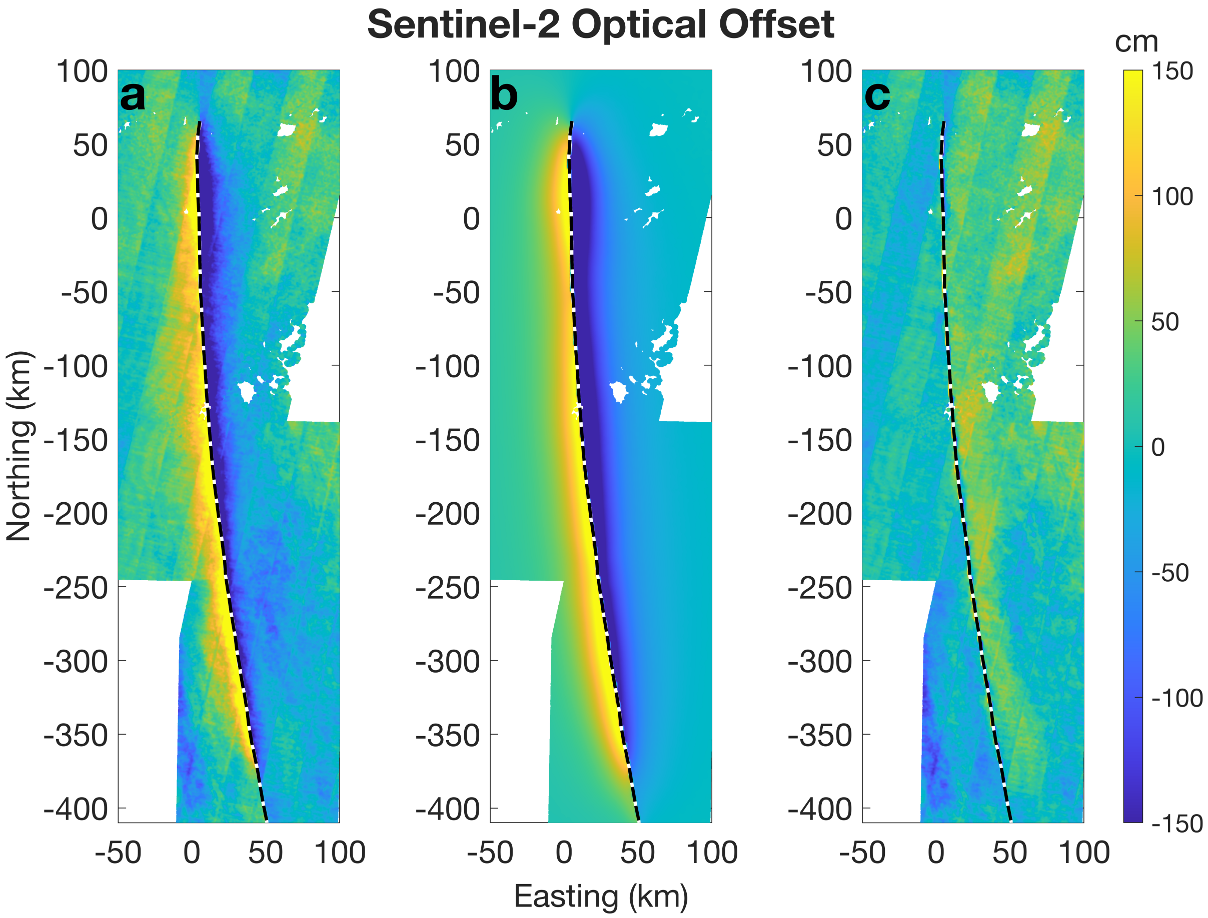

Fig. S19: (a) North-South component of pixel offsets from cross-correlation of Sentinel-2 optical imagery (not used in the inversion for the static slip model). (b) Prediction of the preferred slip model (Fig. S9). (c) Residuals. The dashed line denotes the rupture trace.

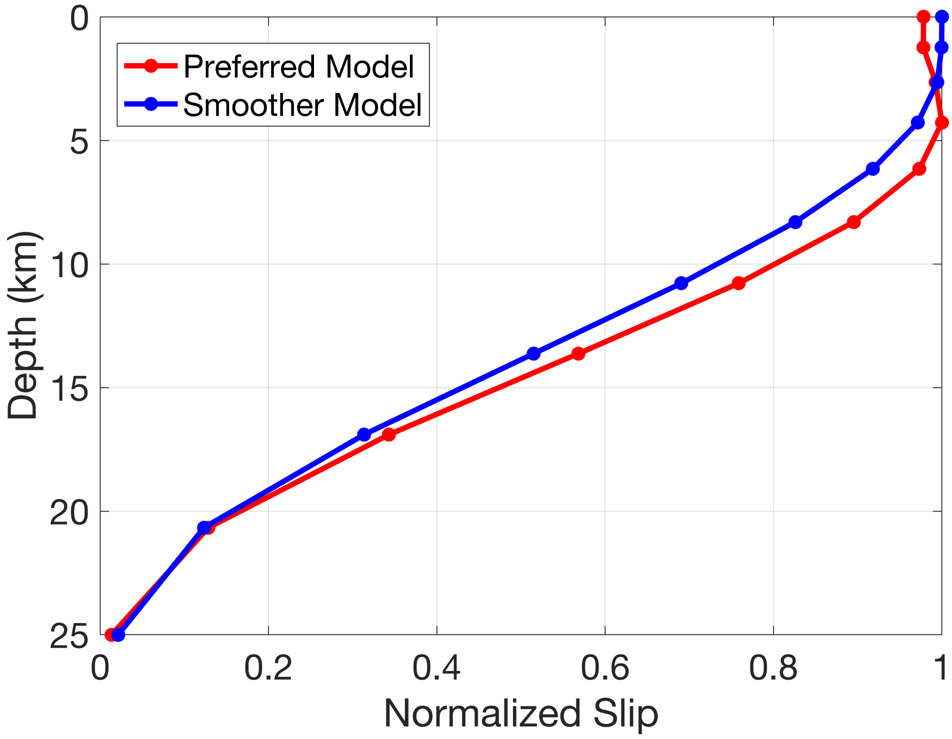

Fig. S20: Along-strike averaged slip as a function of depth. Slip is normalized by the maximum value. Red line: preferred model; blue line: a smoother model (see Fig S7 for the respective smoothness parameters). Both models fit the data equally well.

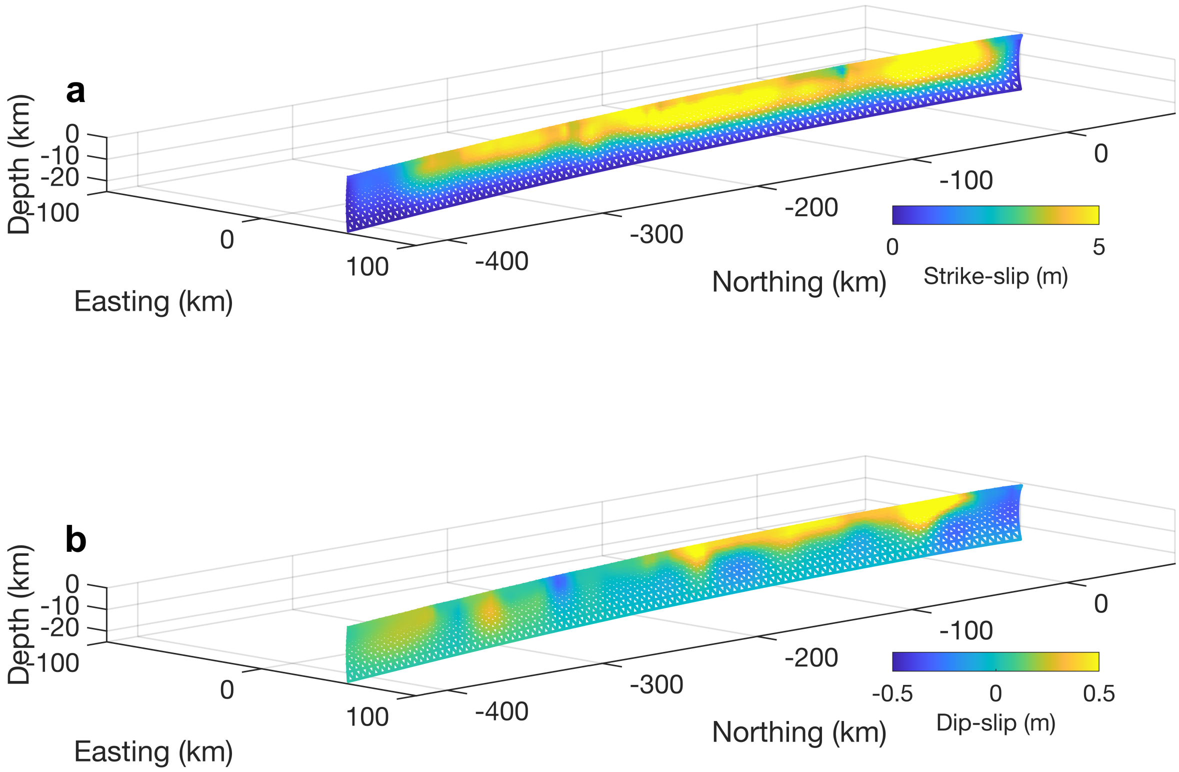

Fig. S21: Static slip distribution for a model assuming a vertical fault. Panel a: strike-slip; Panel b: dip-slip. Right-lateral strike slip and west-side-up dip slip are deemed positive.

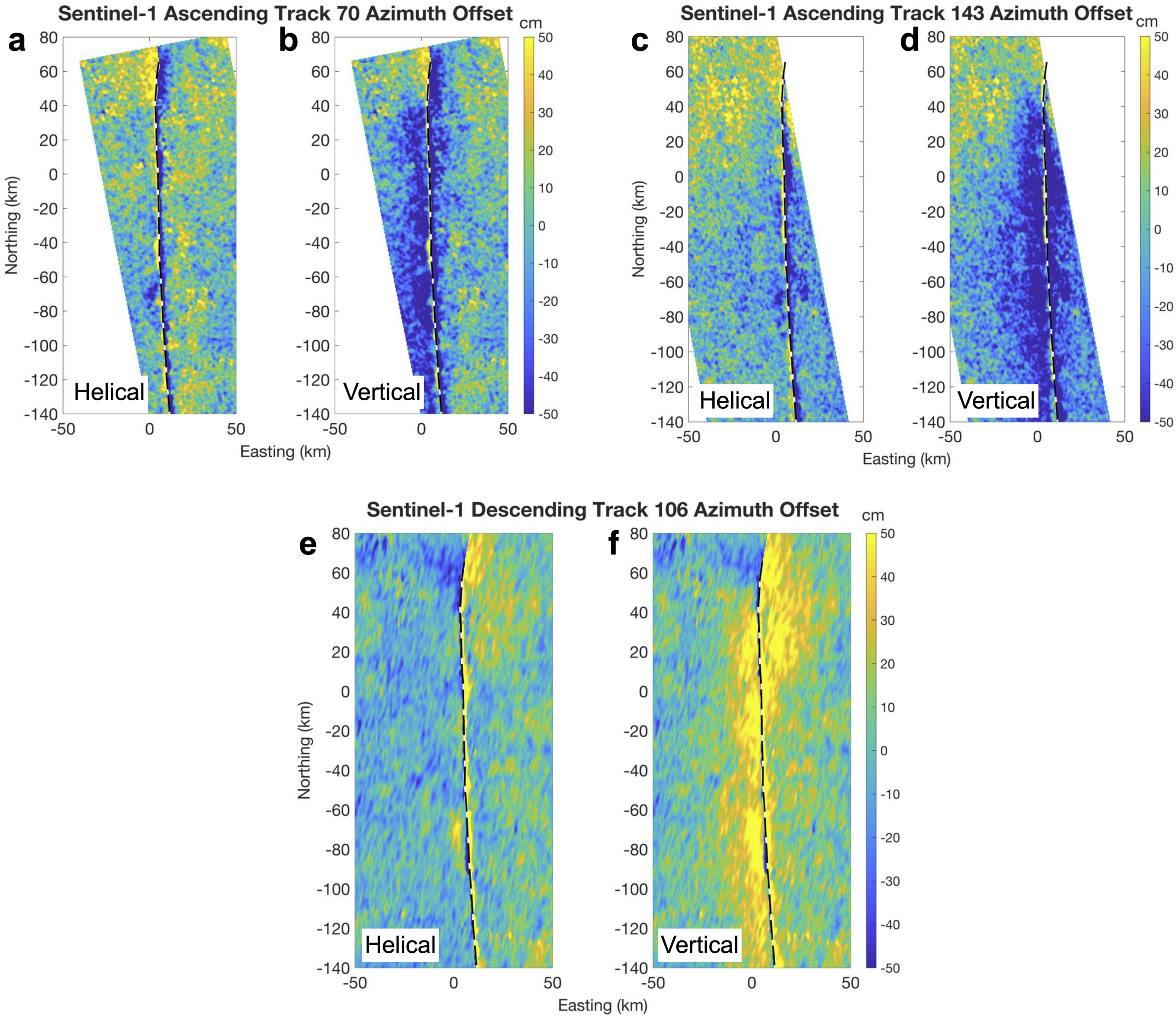

Fig. S22: A comparison between azimuth offset residuals for models with helical and vertical fault geometry. Shown are Sentinel-1A tracks with the largest residuals. The residuals are zoomed in on parts of the rupture where the difference is most notable.

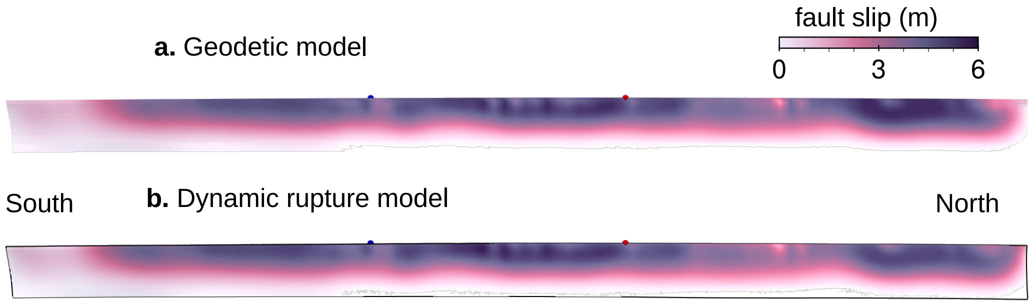

Fig. S23: Comparison of fault slip distributions in the geodetic model (a) and the preferred dynamic rupture model (b).

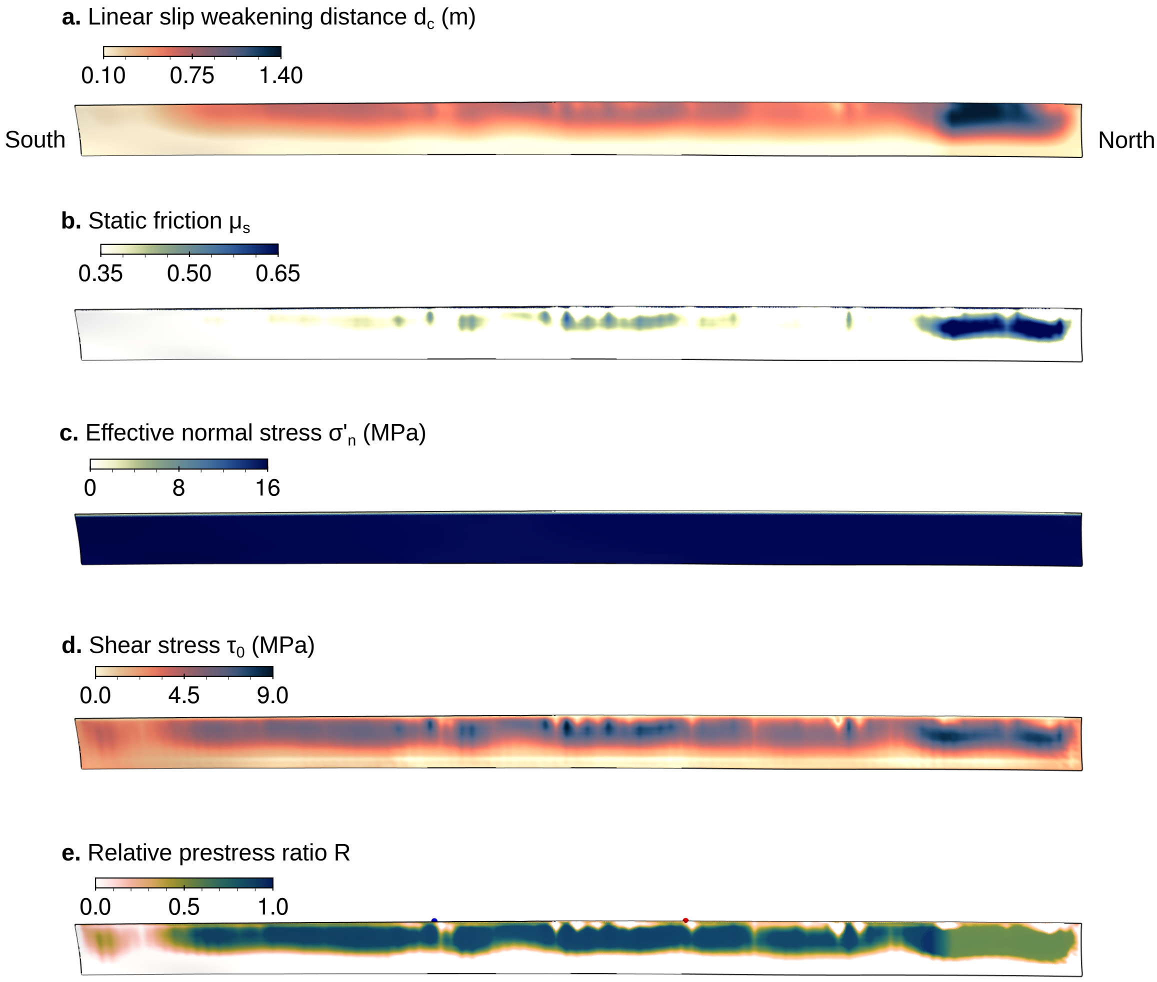

Fig. S24: Distribution of fault friction parameters and prestress in the preferred dynamic rupture model. (a) Slip-weakening distance d_c, scaled proportionally to fault slip. (b) Static friction coefficient μ_s, set to 0.35 and increased in regions of high shear stress, up to a maximum of 0.65. (c) Depth-dependent effective normal stress, increasing linearly from 1 MPa at the surface to 16 MPa at 1.5km depth, constant below. (d) Initial fault shear stress τ_0, derived from the stress change in the finite-fault model and the dynamic strength. (e) Relative prestress ratio R (e.g.,[54]), relating the potential stress drop $\tau_0 - \tau_d$ to the frictional strength drop $\tau_s - \tau_d$, and quantifying fault criticality.

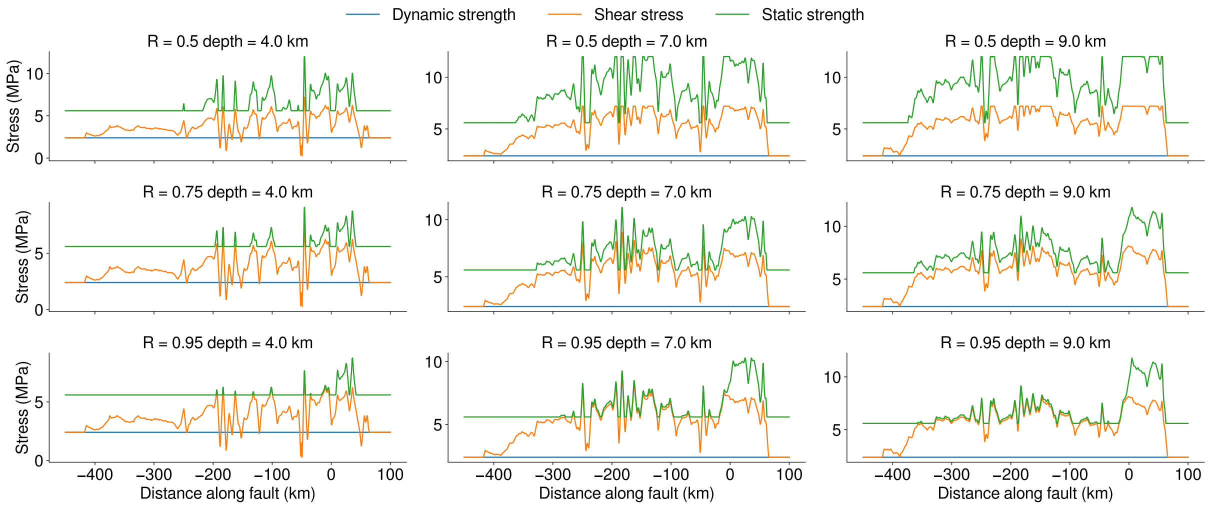

Fig. S25: Depth-dependent profiles of shear stress and fault strengths along the fault for three relative prestress ratio R_{param}: $R_{\text{param}} = 0.5, 0.75$ and 0.95 (preferred model), evaluated at depths of 4 km, 7 km, and 9 km, assuming B=0.95 (preferred model). Each subplot shows shear stress (orange), static strength (green), and dynamic strength (blue) as functions of the y (north–south) coordinate along the fault. The profiles illustrate how μ_s is locally increased above its background value 0.35 to enforce the prescribed R, and also highlight the effect of the background μ_s value on fault criticality.

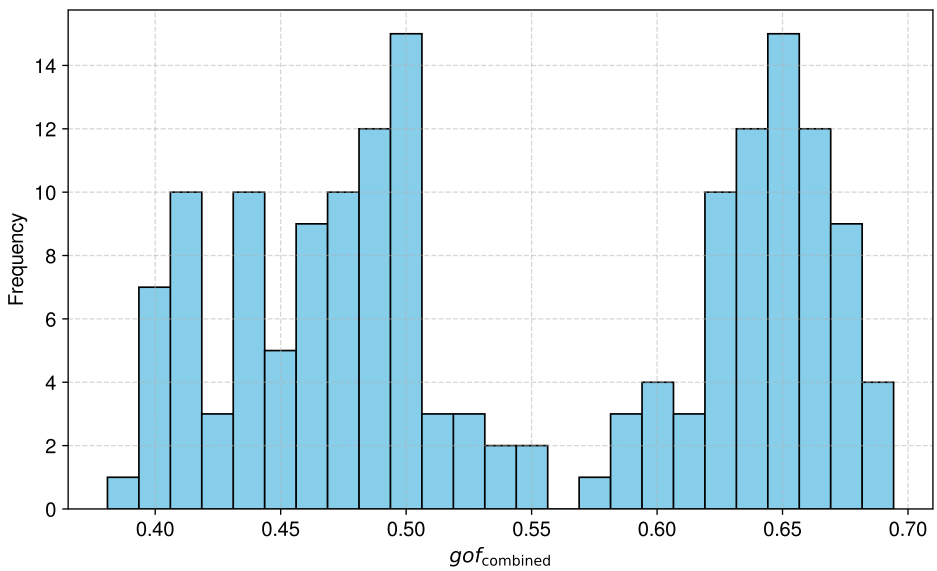

Fig. S26: Histogram of the combined goodness-of-fit values across the dynamic rupture ensemble consisting of 180 models.

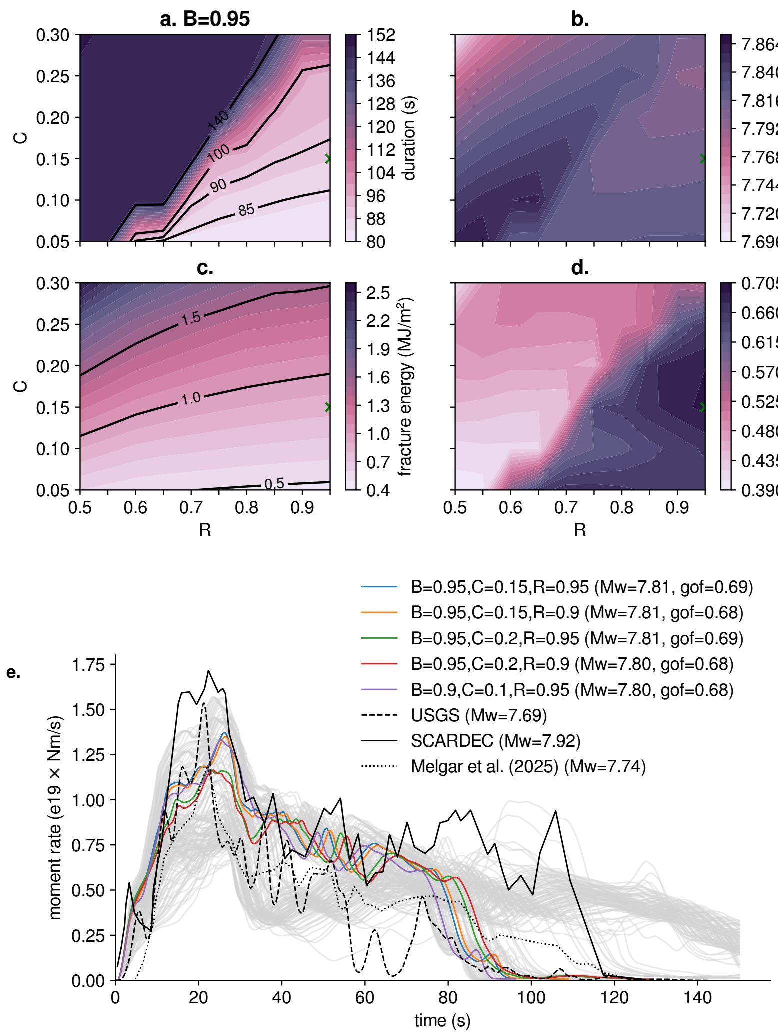

Fig. S27: Dynamic rupture simulation ensemble. Ensemble results across 60 dynamic rupture simulations with varying slip weakening distance (C) and relative prestress ratio (R), while keeping $B = 0.95$ fixed. (a) Rupture duration. (b) Moment magnitude. (c) Fracture energy (in $\mathrm{MJ/m^2}$). (d) Combined goodness of fit (GOF) score. (e) Moment rate functions (MRFs): All 180 simulated MRFs are plotted. The 5 best-fitting models based on combined GOF are highlighted in color and indexed in the legend. The blue curve represents the preferred model. The remaining 175 models are shown in grey. For comparison, the SCARDEC source time function [70] and source time functions from two kinematic models [69;71] are also shown.

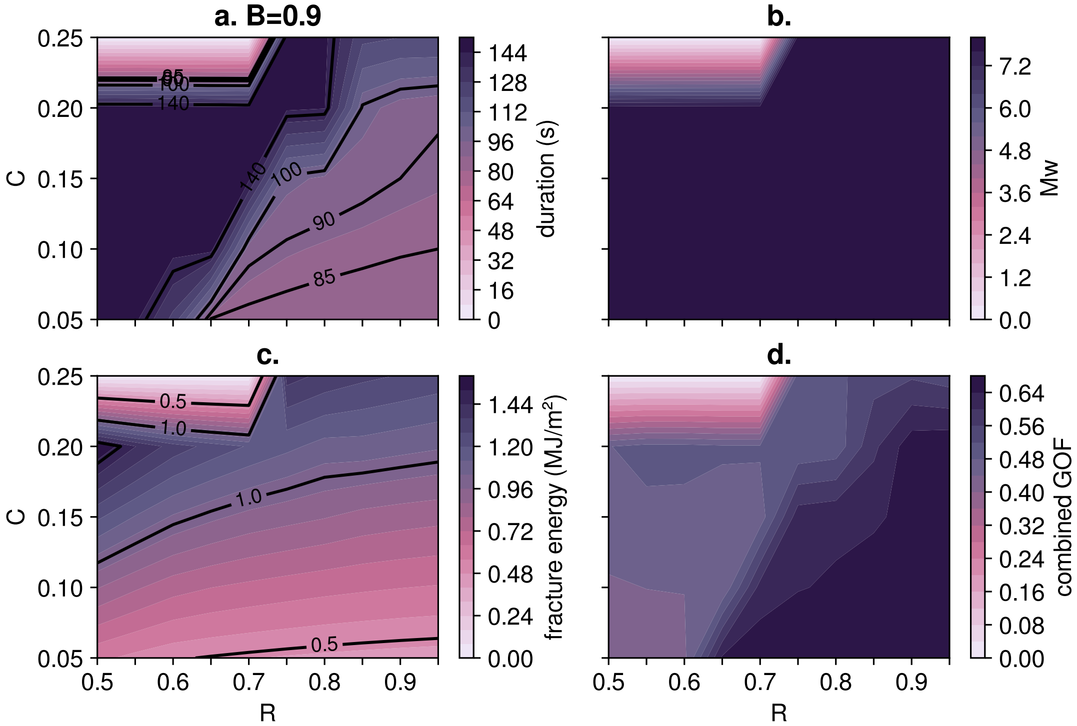

Fig. S28: Dynamic rupture simulation ensemble for $B = 0.9$. Ensemble results across 60 dynamic rupture simulations with varying slip weakening distance (C) and prestress ratio (R), while keeping $B = 0.9$ fixed. (a) Rupture duration. (b) Moment magnitude. (c) Fracture energy (in $\mathrm{MJ/m^2}$). (d) Combined goodness of fit (GOF) score.

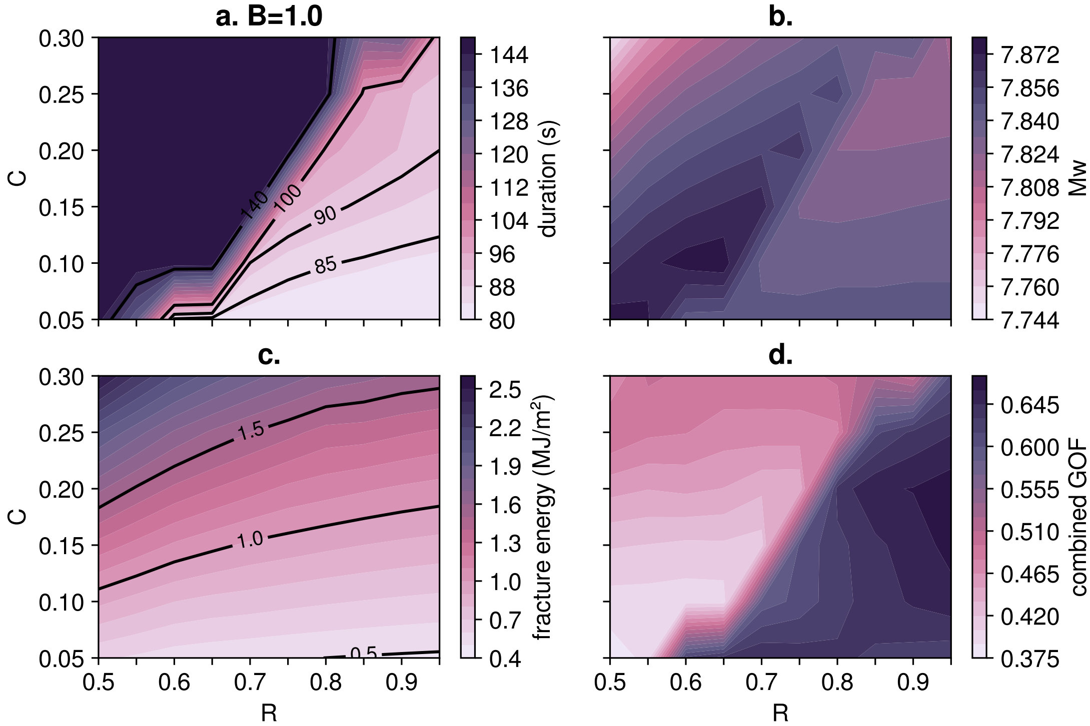

Fig. S29: Dynamic rupture simulation ensemble for $B = 1.0$. Ensemble results across 60 dynamic rupture simulations with varying slip weakening distance (C) and prestress ratio (R), while keeping $B = 1.0$ fixed. (a) Rupture duration. (b) Moment magnitude. (c) Fracture energy (in $\mathrm{MJ/m^2}$). (d) Combined goodness of fit (GOF) score.

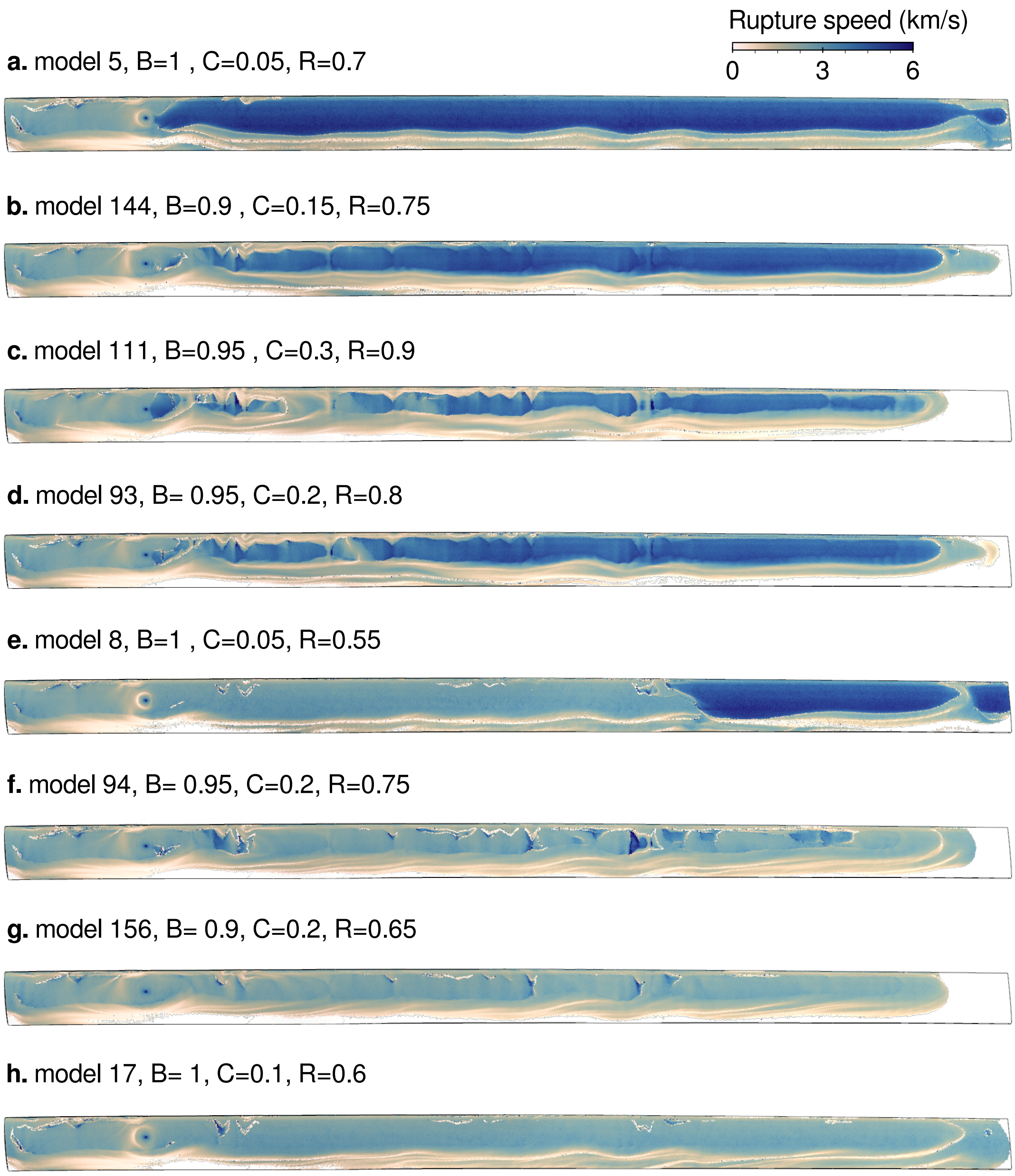

Fig. S30: Rupture speed in selected models from the dynamic rupture simulation ensemble, showing wide variability from fully subshear, through piecewise supershear, to fully supershear rupture.

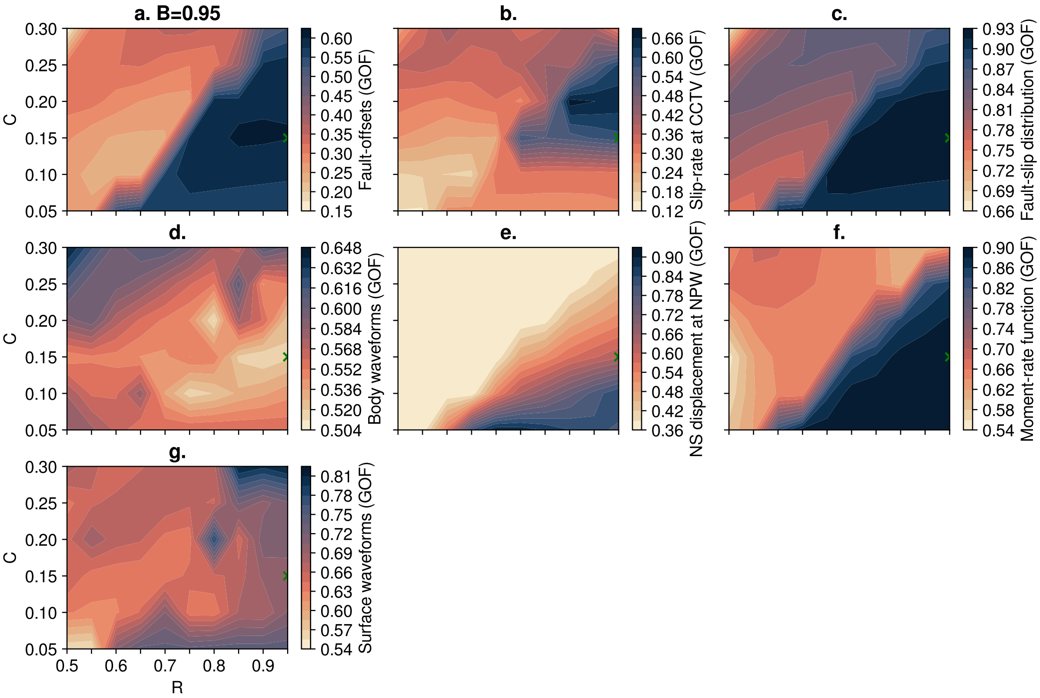

Fig. S31: Goodness-of-fit (GOF) variations for selected observational constraints at fixed $B = 0.95$. Each panel shows ensemble results from 60 dynamic rupture simulations with varying slip weakening distance (C) and prestress ratio (R). Metrics shown: (a) fit to fault offsets; (b) fit to slip-rate at CCTV[73]; (c) fit to fault-slip distribution; (d) fit to teleseismic body waveforms at six stations; (e) fit to north-south displacement at station NPW; (f) fit to the moment-rate function; (g) fit to teleseismic surface waveforms at six stations. The green '×' marker in each panel indicates the parameter combination used in the preferred model.

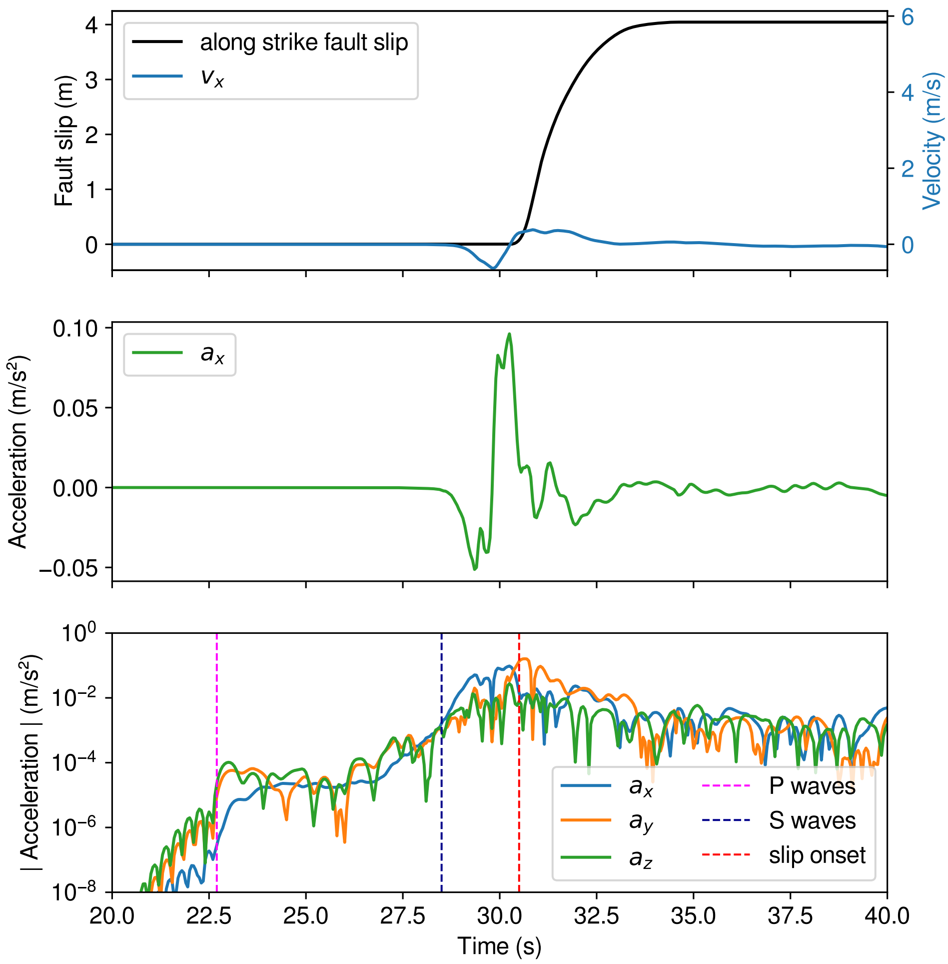

Fig. S32: Modeled ground motion at the CCTV site. Top: Fault slip and east–west ground velocity. Middle: East–west acceleration, showing an eastward pulse preceding local slip, consistent with the gate motion seen in footage and attributed to subshear rupture (supershear would reverse the polarity)[78]. Bottom: Component-wise acceleration amplitudes, with P- and S-wave arrivals preceding the rupture front. The strong shaking in footage 2 s before slip onset has been attributed to S-waves[66;78], supporting locally subshear rupture.

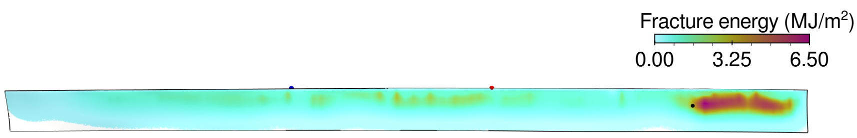

Fig. S33: Distribution of fracture energy in the preferred dynamic rupture model.

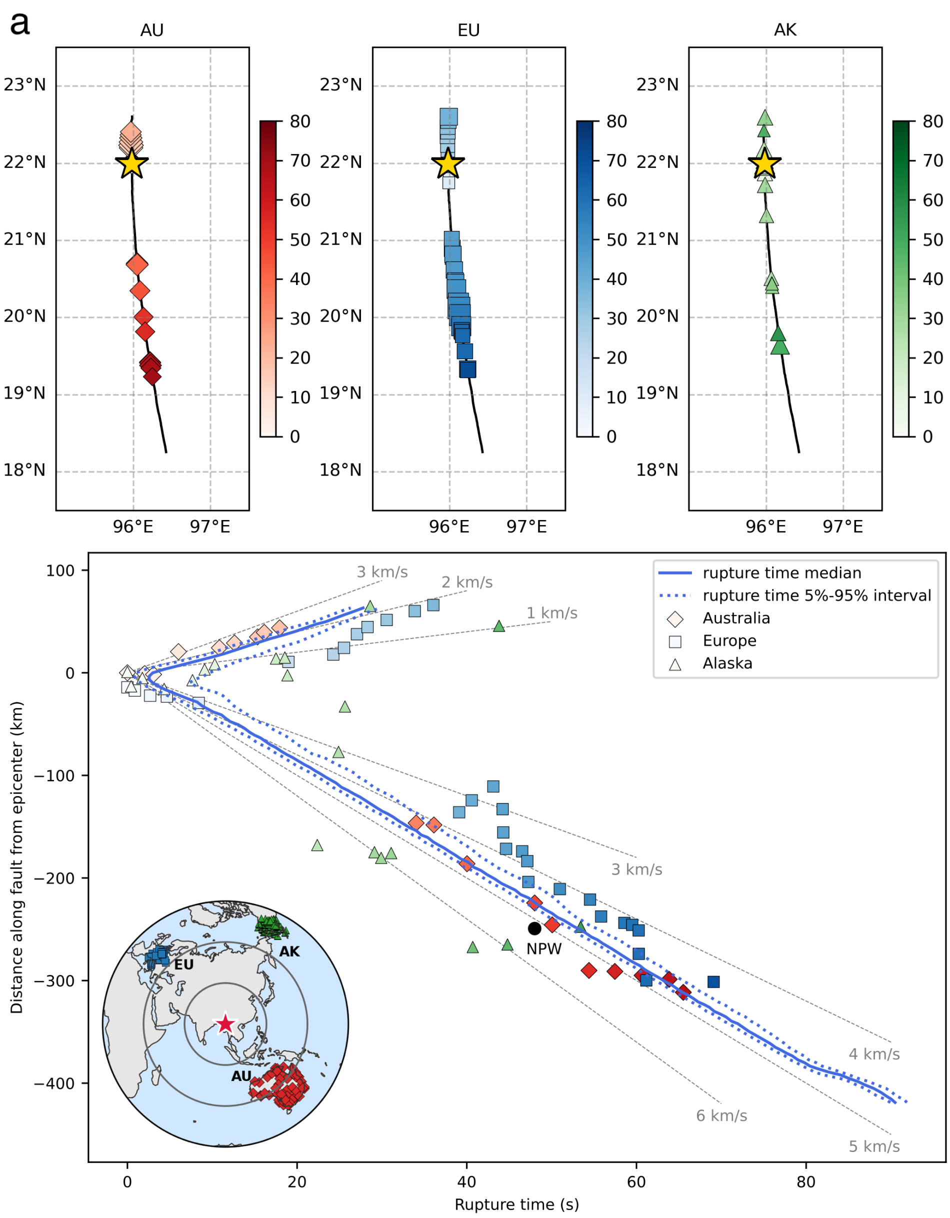

Fig. S34: Teleseismic back projection analysis of the earthquake rupture process. (a) Back projection results from arrays around Australia (red diamonds), Europe (blue squares), and Alaska (green triangles). The color scale represents the rupture time. The size of the markers represents normalized array beam energy. Stars show the epicenter location of the mainshock. (b). Rupture speed from back projection and the preferred dynamic rupture model. Markers are the same as in (a). The black dot represents the location of the NPW station. The solid blue curve represents the median rupture onset time of the preferred dynamic rupture model along the respective along-strike distance. The dotted blue curves indicate the 5% and 95% percentiles of the rupture onset time. The 5% percentile corresponds to the earlier arrival of the rupture front at depth, while the spread between the 5% and 95% percentiles reflects the local curvature of the rupture front. Grey dashed lines show different constant rupture speeds for reference. The inset shows stations and epicenter locations.

13. References

[1] Sandwell, D., Mellors, R., Tong, X., Wei, M. & Wessel, P. Open radar interferometry software for mapping surface deformation. *EOS, Trans. AGU* **92**, 234–234 (2011).

[2] Farr, T. & Kobrick, M. Shuttle Radar Topography Mission produces a wealth of data. *AGU Eos* **81**, 583–585 (2000).

[3] D'Errico, J. Surface fitting using gridfit (2025). URL https://www.mathworks.com/matlabcentral/fileexchange/8998-surface-fitting-using-gridfit.

[4] Goldstein, R. M., Zebker, H. A. & Werner, C. L. Satellite radar interferometry: two-dimensional phase unwrapping. *Radio science* **23**, 713–720 (1988).

[5] Simons, M., Fialko, Y. & Rivera, L. Coseismic deformation from the 1999 Mw 7.1 Hector Mine, California, earthquake as inferred from InSAR and GPS observations. *bssa* **92**, 1390–1402 (2002).

[6] Jonsson, S., Zebker, H., Segall, P. & Amelung, F. Fault slip distribution of the 1999 M_w 7.1 Hector Mine, California, earthquake, estimated from satellite radar and GPS measurements. *Bull. Seism. Soc. Am.* **92**, 1377–1389 (2002).

[7] Wang, K. & Fialko, Y. Slip model of the 2015 M_w 7.8 Gorkha (Nepal) earthquake from inversions of ALOS-2 and GPS data. *Geophys. Res. Lett.* **42**, 7452–7458 (2015).

[8] Ayoub, F., Leprince, S. & Keene, L. User's guide to COSI-CORR co-registration of optically sensed images and correlation. *California Institute of Technology: Pasadena, CA, USA* **38**, 49s (2009).

[9] Leprince, S., Ayoub, F., Klinger, Y. & Avouac, J.-P. Co-Registration of optically sensed images and correlation (COSI-Corr): an operational methodology for ground deformation measurements. In *2007 IEEE International Geoscience and Remote Sensing Symposium*, 1943–1946 (2007).

[10] Aati, S., Milliner, C. & Avouac, J.-P. A new approach for 2-D and 3-D precise measurements of ground deformation from optimized registration and correlation of optical images and ICA-based filtering of image geometry artifacts. *Remote Sensing of Environment* **277**, 113038 (2022).

[11] Fialko, Y., Simons, M. & Agnew, D. The complete (3-D) surface displacement field in the epicentral area of the 1999 M_w7.1 Hector Mine earthquake, southern California, from space geodetic observations. *Geophys. Res. Lett.* **28**, 3063–3066 (2001).

[12] Fialko, Y. & Jin, Z. Simple shear origin of the cross-faults ruptured in the 2019 Ridgecrest earthquake sequence. *Nature Geoscience* **14**, 513–518 (2021).

[13] Wang, X. *et al.* A 3-D shear wave velocity model for Myanmar region. *Journal of Geophysical Research: Solid Earth* **124**, 504–526 (2019).

[14] Brocher, T. M. Empirical relations between elastic wavespeeds and density in the earth's crust. *Bulletin of the seismological Society of America* **95**, 2081–2092 (2005).

[15] Jin, Z., Zou, X., Wang, K. & Fialko, Y. SlipSolve: Geodetic Linear Inversion (2025). URL https://github.com/ZeyuJin/geodetic_inversion.

[16] Wang, R., Martin, F. & Roth, F. Computation of deformation induced by earthquakes in a multi-layered elastic crust - FORTRAN programs EDGRN/EDCMP. *Comp. Geosci.* **29**, 195–207 (2003).

[17] Jin, Z., Fialko, Y., Yang, H. & Li, Y. Transient deformation excited by the 2021 M7.4 Maduo (China) earthquake: Evidence of a deep shear zone. *J. Geophys. Res.* **128**, e2023JB026643 (2023).

[18] Jin, Z., Fialko, Y., Zubovich, A. & Schöne, T. Lithospheric deformation due to the 2015 M7.2 Sarez (Pamir) earthquake constrained by 5 years of space geodetic observations. *J. Geophys. Res.* **127**, e2021JB022461 (2022).

[19] Okada, Y. Surface deformations due to shear and tensile faults in a halfspace. *Bull. Seism. Soc. Am.* **75**, 1135–1154 (1985).

[20] Meade, B. J. AlgorithMs for the calculation of exact displacements, strains, and stresses for triangular dislocation elements in a uniform elastic half space. *Computers & geosciences* **33**, 1064–1075 (2007).

[21] Nikkhoo, M. & Walter, T. R. Triangular dislocation: an analytical, artefact-free solution. *Geophysical Journal International* **201**, 1119–1141 (2015).

[22] Fialko, Y. Probing the mechanical properties of seismically active crust with space geodesy: Study of the co-seismic deformation due to the 1992 M_w7.3 Landers (southern California) earthquake. *J. Geophys. Res.* **109**, B03307, 10.1029/2003JB002756 (2004).

[23] Zienkiewicz, O. *The finite element method* (McGraw-Hill Book Company, London, 1977), 3 edn.

[24] Golub, G. H., Hansen, P. C. & O'Leary, D. P. Tikhonov regularization and total least squares. *SIAM journal on matrix analysis and applications* **21**, 185–194 (1999).

[25] Meyer, M., Desbrun, M., Schröder, P. & Barr, A. H. Discrete differential-geometry operators for triangulated 2-manifolds. In *Visualization and mathematics III*, 35–57 (Springer, 2003).

[26] Voronoi, G. Nouvelles applications des paramètres continus à la théorie des formes quadratiques. deuxième mémoire. recherches sur les parallélloèdres primitifs. *Journal für die reine und angewandte Mathematik (Crelles Journal)* **1908**, 198–287 (1908).

[27] Devroye, L., Györfi, L., Lugosi, G. & Walk, H. On the measure of voronoi cells. *Journal of Applied Probability* **54**, 394–408 (2017).

[28] Jin, Z. & Fialko, Y. Finite slip models of the 2019 Ridgecrest earthquake sequence constrained by space geodetic data and aftershock locations. *Bull. Seism. Soc. Am.* **110**, 1660–1679 (2020).

[29] Ulrich, T., Magen, Y. & Gabriel, A.-A. The complex rupture dynamics of an oceanic transform fault: supershear rupture and deep slip during the 2024 Mw7. 0 cape mendocino earthquake. Preprint at EarthArXiv (2025).

[30] Gabriel, A.-A. *et al.* SeisSol (2025). URL https://doi.org/10.5281/zenodo.15685917.

[31] Käser, M., Hermann, V. & Puente, J. d. l. Quantitative accuracy analysis of the discontinuous galerkin method for seismic wave propagation. *Geophysical Journal International* **173**, 990–999 (2008).

[32] Dumbser, M. & Käser, M. An arbitrary high-order discontinuous Galerkin method for elastic waves on unstructured meshes—II. The three-dimensional isotropic case. *Geophysical Journal International* **167**, 319–336 (2006).

[33] Breuer, A. *et al.* Sustained Petascale Performance of Seismic Simulations with SeisSol on SuperMUC. In *Supercomputing. ISC 2014. Lecture Notes in Computer Science, vol 8488*, 1–18 (Springer, 2014).

[34] Heinecke, A. *et al.* Petascale high order dynamic rupture earthquake simulations on heterogeneous supercomputers. In *SC'14: International Conference for High-Performance Computing, Networking, Storage and Analysis* (2014).

[35] Rettenberger, S., Meister, O., Bader, M. & Gabriel, A.-A. ASAGI: A Parallel Server for Adaptive Geoinformation. In *Proceedings of the Exascale applications and Software Conference 2016*, EASC '16, 2:1–2:9 (ACM, New York, NY, USA, 2016).

[36] Uphoff, C. *et al.* Extreme scale multi-physics simulations of the tsunamigenic 2004 Sumatra megathrust earthquake. In *Proceedings of the International Conference for High Performance Computing, networking, Storage and Analysis, SC 2017* (2017).

[37] Krenz, L. *et al.* 3D acoustic-elastic coupling with gravity: the dynamics of the 2018 Palu, Sulawesi earthquake and tsunami. In *Proceedings of the International Conference for High-Performance Computing, Networking, Storage and Analysis*, SC '21 (ACM, New York, NY, USA, 2021).

[38] Pelties, C., Gabriel, A.-A. & Ampuero, J.-P. Verification of an ADER-DG method for complex dynamic rupture problems. *Geoscientific Model Development* **7**, 847–866 (2014).

[39] Harris, R. A. *et al.* A suite of exercises for verifying dynamic earthquake rupture codes. *Seismol. Res. Lett.* **89**, 1146–1162 (2018).

[40] Vyas, J. C., Gabriel, A., Ulrich, T., Mai, P. M. & Ampuero, J. How does thermal pressurization of pore fluids affect 3D strike-slip earthquake dynamics and ground motions? *Bulletin of the Seismological Society of America* **113**, 1992–2008 (2023).

[41] Ida, Y. Cohesive force across the tip of a longitudinal-shear crack and griffith's specific surface energy. *Journal of Geophysical Research* **77**, 3796–3805 (1972).

[42] Andrews, D. Rupture propagation with finite stress in antiplane strain. *Journal of Geophysical Research* **81**, 3575–3582 (1976).
[43] Day, S. M., Yu, G. & Wald, D. J. Dynamic stress changes during earthquake rupture. *Bulletin of the Seismological Society of America* **88**, 512–522 (1998).
[44] Tinti, E., Spudich, P. & Cocco, M. Earthquake fracture energy inferred from kinematic rupture models on extended faults. *Journal of Geophysical Research: Solid Earth* **110** (2005).
[45] Causse, M., Dalguer, L. A. & Mai, P. M. Variability of dynamic source parameters inferred from kinematic models of past earthquakes. *Geophysical Journal International* **196**, 1754–1769 (2014).
[46] Yang, H., Yao, S., He, B., Newman, A. V. & Weng, H. Deriving rupture scenarios from interseismic locking distributions along the subduction megathrust. *Journal of Geophysical Research: Solid Earth* **124**, 10376–10392 (2019).
[47] Tinti, E. *et al.* Constraining families of dynamic models using geological, geodetic and strong ground motion data: The Mw 6.5, October 30th, 2016, Norcia earthquake, Italy. *Earth and Planetary Science Letters* **576**, 117237 (2021).
[48] Jia, Z. *et al.* The complex dynamics of the 2023 Kahramanmaraş, Turkey, M_w 7.8-7.7 earthquake doublet. *Science* **381**, 985–990 (2023).
[49] Glehman, J. *et al.* Partial ruptures governed by the complex interplay between geodetic slip deficit, rigidity, and pore fluid pressure in 3D cascadia dynamic rupture simulations. *Seismica* **2** (2025).
[50] Marchandon, M. *et al.* Forecasting 3D rupture dynamics of the alto tiberina Low-Angle normal fault, italy. *Seismica* **4** (2025).
[51] Day, S. M., Dalguer, L. A., Lapusta, N. & Liu, Y. Comparison of finite difference and boundary integral solutions to Three-Dimensional spontaneous rupture. *Journal of Geophysical Research: Solid Earth* **110** (2005).
[52] Kammer, D. S. *et al.* Earthquake energy dissipation in a fracture mechanics framework. *Nature Communications* **15**, 4736 (2024).
[53] Wollherr, S., Gabriel, A.-A. & Uphoff, C. Off-fault plasticity in three-dimensional dynamic rupture simulations using a modal Discontinuous Galerkin method on unstructured meshes: Implementation, verification and application. *Geophys. J. Int.* **214**, 1556–1584 (2018).
[54] Aochi, H. & Madariaga, R. The 1999 İzmit, Turkey Earthquake: nonplanar pault sructure, dynamic rupture process, and strong ground motion. *Bulletin of the Seismological Society of America* **93**, 1249–1266 (2003).
[55] Ulrich, T., Gabriel, A.-A., Ampuero, J.-P. & Xu, W. Dynamic viability of the 2016 Mw 7.8 Kaikōura earthquake cascade on weak crustal faults. *Nature Communications* **10** (2019).
[56] Suppe, J. Fluid overpressures and strength of the sedimentary upper crust. *Journal of Structural Geology* **69**, 481–492 (2014).
[57] Weng, H. & Yang, H. Constraining frictional properties on fault by dynamic rupture simulations and near-field observations. *Journal of Geophysical Research: Solid Earth* **123**, 6658–6670 (2018).
[58] Galis, M. *et al.* On the initiation of sustained Slip-Weakening ruptures by localized stresses. *Geophysical Journal International* **200**, 890–909 (2015).
[59] USGS. Origin information for the M 7.7 2025 Mandalay, Burma (Myanmar) earthquake (2025). URL https://earthquake.usgs.gov/earthquakes/eventpage/us7000pn9s/origin/detail. Last accessed: 2025-07-08.
[60] Cocco, M. *et al.* Fracture energy and breakdown work during earthquakes. *Annual Review of Earth and Planetary Sciences* **51**, 217–252 (2023).
[61] Ide, S. & Aochi, H. Earthquakes as multiscale dynamic ruptures with heterogeneous fracture surface energy. *Journal of Geophysical Research: Solid Earth* **110** (2005).
[62] Gabriel, A.-A., Garagash, D. I., Palgunadi, K. H. & Mai, P. M. Fault size–dependent fracture energy explains multiscale seismicity and cascading earthquakes. *Science* **385**, eadj9587 (2024).

[63] Kaneko, Y., Fukuyama, E. & Hamling, I. J. Slip-Weakening distance and energy budget inferred from near-fault ground deformation during the 2016 Mw7.8 Kaikōura earthquake. *Geophysical Research Letters* **44**, 4765–4773 (2017).

[64] Gallovič, F. *et al.* Complex rupture dynamics on an immature fault during the 2020 Mw 6.8 Elazığ earthquake, Turkey. *Communications Earth & Environment* **1**, 1–8 (2020).

[65] Gallovič, F., Valentová, Ľ., Ampuero, J.-P. & Gabriel, A.-A. Bayesian Dynamic Finite-Fault Inversion: 2. Application to the 2016 Mw 6.2 Amatrice, Italy, Earthquake. *Journal of Geophysical Research: Solid Earth* **124**, 6970–6988 (2019).

[66] Kearse, J. & Kaneko, Y. Curved Fault slip captured by CCTV video during the 2025 Mw 7.7 Myanmar Earthquake. *The Seismic Record* **5**, 281–288 (2025).

[67] Fukuyama, E. & Mikumo, T. Slip-Weakening distance estimated at near-fault stations. *Geophysical Research Letters* **34** (2007).

[68] Wong, J. W. C., Fan, W. & Gabriel, A.-A. A quantitative comparison and validation of Finite-Fault models: the 2011 Tohoku-Oki earthquake. *Journal of Geophysical Research: Solid Earth* **129**, e2024JB029212 (2024).

[69] USGS. Finite Fault model of the M 7.7 2025 Mandalay, Burma (Myanmar) earthquake (2025). URL https://earthquake.usgs.gov/earthquakes/eventpage/us7000pn9s/executive. Last accessed: 2025-07-08.

[70] Vallée, M., Charléty, J., Ferreira, A. M. G., Delouis, B. & Vergoz, J. SCARDEC: A new technique for the rapid determination of seismic moment magnitude, focal mechanism and source time functions for large earthquakes using body-wave deconvolution. *Geophysical Journal International* **184**, 338–358 (2011).

[71] Melgar, D. *et al.* Supershear source model of the 2025 M7.8 Myanmar earthquake and paleoseismology of the Sagaing fault: regions of significant overlap with past earthquakes. *Seismica* **4** (2025).

[72] Lai, S.-T. *et al.* Capacity building enables unique near-fault observations of the destructive 2025 M_w 7.7 Myanmar earthquake. *Earth System Science Data Discussions* **2025**, 1–23 (2025).

[73] Latour, S. *et al.* Direct estimation of earthquake source properties from a single CCTV camera. Preprint at EarthArXiv (2025).

[74] Ishii, M., Shearer, P. M., Houston, H. & Vidale, J. E. Extent, duration and speed of the 2004 Sumatra–Andaman earthquake imaged by the Hi-Net array. *Nature* **435**, 933–936 (2005).

[75] Tan, F., Ge, Z., Kao, H. & Nissen, E. Validation of the 3-D phase-weighted relative back projection technique and its application to the 2016 Mw 7.8 Kaikōura earthquake. *Geophysical Journal International* **217**, 375–388 (2019). Publisher: Oxford Academic.

[76] Kennett, B. L. N. & Engdahl, E. R. Traveltimes for global earthquake location and phase identification. *Geophysical Journal International* **105**, 429–465 (1991).

[77] Kundu, B. & Gahalaut, V. Earthquake occurrence processes in the Indo-Burmese wedge and Sagaing Fault Region. *Tectonophysics* **524-525**, 135–146 (2012).

[78] Hirano, S., Doke, R. & Maeda, T. Supershear-Subshear-Supershear rupture sequence during the 2025 Mandalay earthquake in Myanmar. Preprint at EarthArXiv (2025). URL https://doi.org/10.26443/seismica.v4i2.1785.